High order conservative Lagrangian schemes for two-dimensional radiation hydrodynamics equations in the equilibrium-diffusion limit

Nuo Lei[1], Juan Cheng[2] and Chi-Wang Shu[3]

Abstract

Radiation hydrodynamics equations (RHE) refer to the study of how interactions between radiation and matter influence thermodynamic states and dynamic flow, which has been widely applied to high temperature hydrodynamics, such as inertial confinement fusion (ICF) and astrophysical gaseous stars. Solving RHE accurately and robustly even under the equilibrium diffusion approximation is a challenging task. To address this, we develop two types of high order conservative Lagrangian schemes for RHE in the equilibrium-diffusion limit for the two dimensional case on the Lagrangian moving mesh. Based on the multi-resolution WENO reconstruction for the spatial discretization and strong stability preserving Runge-Kutta (SSP-RK) time discretization, we first develop an explicit Lagrangian scheme with the HLLC numerical flux to achieve high order accuracy in space and time. We also discuss the positivity-preserving property of the high order explicit Lagrangian scheme. To overcome the severe time step restriction arising from the nonlinear radiation diffusion term in the explicit scheme, we further present a high order explicit-implicit-null (EIN) Lagrangian scheme. By adding a sufficiently large linear diffusion term on both sides of the scheme, we treat the complicated nonlinear parts explicitly and efficiently, and treat the added linear diffusion term on the right-hand side implicitly with a relaxed time step restriction. According to our numerical experiments, these two types of Lagrangian schemes are high order accurate, conservative and can capture the interfaces automatically. Additionally, the explicit scheme is found to be non-oscillatory and can preserve positivity while maintaining the original high order accuracy.

Keywords: Lagrangian method; High-order; Positivity-preserving; Radiation hydrodynamics equations; Equilibrium-diffusion limit; Explicit-implicit-null time discretization.

[1]Graduate School, China Academy of Engineering Physics, Beijing 100088, China. E-mail: leinuo19@gscaep.ac.cn.

[2]Corresponding author. Laboratory of Computational Physics, Institute of Applied Physics and Computational Mathematics, Beijing 100088, China and HEDPS, Center for Applied Physics and Technology, and College of Engineering, Peking University, Beijing 100871, China. E-mail: cheng_juan@iapcm.ac.cn. Research is supported in part by NSFC grant 12031001, and National Key R&D Program of China No. 2022YFA1004500.

[3]Division of Applied Mathematics, Brown University, Providence, RI 02912. E-mail: chi-wang_shu@brown.edu. Research is supported in part by NSF grant DMS-2010107.

1 Introduction

Radiation hydrodynamics (RH) is a research field focusing on the interactions between radiation and matter, which can significantly affect the thermodynamic states and dynamic flow characteristics of the matter-radiation system. The radiation hydrodynamics equations (RHE) are a set of partial differential equations that describe the transfer of energy and momentum between radiation and matter, and they are critical for understanding a range of phenomena, such as astrophysical gaseous stars, reentry vehicles, fusion physics, and inertial confinement fusion (ICF), since radiation plays an important role in energy transfer.

However, the full RH equations are computationally expensive to solve, thus various model approximations have been developed, such as the equilibrium diffusion approximation (EDA) [15, 8]. This approximation has four basic assumptions: the system is much larger than the photon mean-free-path, the radiation is in thermal equilibrium with the material, the radiation flux is diffusive, and the radiation pressure is isotropic. In the equilibrium-diffusion limit, the radiation variables are explicit functions of the hydrodynamic variables, and RHE can be described as a hyperbolic system with a nonlinear radiative heat transfer term. This approximation provides a useful way to solve the radiation hydrodynamics equations and obtain insights into the complex interactions between radiation and matter in a variety of settings, including fusion-dominated energy sources, diverse astrophysical settings, and high-energy-density physics.

Although the equilibrium-diffusion limit provides a simplified framework for solving radiation hydrodynamics equations, challenges still exist. Firstly, due to the strong coupling between radiation and hydrodynamics, the difference between their characteristic time scales can cause a stability issue, as their time scales differ by several orders of magnitude. Secondly, as with the usual hydrodynamics problems, numerical schemes would require high resolution near discontinuities and would need to avoid spurious numerical oscillations. Thirdly, it is more challenging to maintain certain physical properties, such as conservation and positivity-preserving for physical variables like density, internal energy, and temperature in

RHE. Fourthly, while many high-order numerical methods have been developed for solving either the Euler equations or radiation diffusion equations, there are few publications that extend these methods to the coupled system of RHE. Lastly, RHE is commonly used to depict interactions between radiation and multi-material matter in ICF, thus making it crucial to capture material interfaces accurately. These complexities pose a challenge to accurately solve RHE and predict the behavior of RHE.

There are some works on solving RHE accurately. In [2], the authors compared three explicit-implicit schemes for solving RHE in the equilibrium diffusion limit. Restricted to the "low-energy-density" regime, fluid pressure and energy density significantly outweigh effects of radiation pressure and energy density which can be ignored. So, a fully second order self-consistent implicit/explicit time integration method was developed for solving radiation hydrodynamics and hydrodynamics plus heat conduction problems in [11, 10]. They split the RHE operators such that the hydrodynamics part was solved explicitly and the radiation diffusion part was solved implicitly. By using precise information of local speeds of propagation, Qamar and Ashraf's method [17] could reduce numerical diffusion and it achieved second order accuracy in space and time by using the MUSCL-type reconstruction and Runge-Kutta time discretization. In [3], the authors proposed a second-order implicit-explicit (IMEX) method for the one-dimensional RHE in the equilibrium diffusion and streaming limit. MUSCL-Hancock and linear discontinuous Galerkin methods were used for the spatial discretization and the TR/BDF2 method was used for the time integration. The authors in [20, 24] solved the radiation and fluid parts separately, by using the gas-kinetic scheme (GKS) for the hydrodynamics term and the unified gas-kinetic scheme (UGKS) for the non-equilibrium radiative transfer term on the fixed mesh.

All of the above works for RHE are performed on the fixed mesh, and there is little discussion on the moving mesh, which could have higher resolution especially for the contact discontinuities and can capture the interfaces for the multi-material problems automatically. The authors in [12] introduced a novel second-order solver on the unstructured moving

Voronoi meshes for the RHE with the slope-limited linear spatial extrapolation and the first-order time discretization. For the high order schemes on the moving mesh, the authors in [7] proposed explicit-type and IMEX-type finite volume schemes for one-dimensional RHE in the equilibrium-diffusion limit on the Lagrangian moving mesh. Positivity-preserving property for the high order explicit scheme was also discussed. Overall, there is little discussion on high order and positivity-preserving numerical methods for solving RHE on the moving meshes in higher dimensions.

When solving partial differential equations (PDEs), the Lagrangian method [6, 7, 14, 16] focuses on the behavior of individual particles or elements which is different from the Eulerian method focusing on fixed control volume. Lagrangian methods can be employed for a wide range of problems, from simple inviscid flows to complex viscous flows with heat transfer, and it can also be easily extended to problems with multiple fluids. Besides that, Lagrangian methods are well-suited for resolving discontinuities, especially contact discontinuities, in the solution, as it automatically captures the motion of fluid or material interfaces across these regions, so it is very suitable for multi-material problems.

In this paper, we will develop high order and conservative methods on the Lagrangian moving meshes for the 2D RHE in the equilibrium-diffusion limit, building on the work in [7]. The spatial discretization uses a multi-resolution weighted essentially non-oscillatory (WENO) reconstruction [28, 29] based on the information of cell averages, which is conservative, high order accurate in smooth regions and essentially non-oscillatory near discontinuities or sharp gradients. This multi-resolution WENO reconstruction is more convenient than the previous works due to its allowance of arbitrary positive linear weights and simpler nested central stencil combinations. For the time discretization, the scheme adopts a high order SSP-RK method [9], which is a convex combination of Euler forward methods.

Positivity preservation is crucial for solving RHE since some physical variables, including density and total internal energy, are positive. Negative density or internal energy not only violates physics, but also makes the numerical scheme unstable. It is much more difficult

for the high order schemes to preserve positivity than the low order schemes. In this study, we first define an admissible set for conserved physical variables, where density and internal energy are positive if the conserved variables are in this set. We confirm that the initial cell averages are in the admissible set. Then, we prove that our first order explicit Lagrangian scheme with the HLLC numerical flux can preserve positivity under a suitable time step condition. Next, we move forward to the high order scheme. We demonstrate that if the time step meets certain conditions and the input physical values remain in the admissible set, then the cell averages obtained from the explicit Lagrangian scheme also remain in the admissible set, thereby preserving the positivity of density and internal energy. To ensure the input physical values of the high-order reconstruction polynomials are also in the admissible set, we implement the conservative positivity-preserving limiter of Zhang and Shu [25].

The above explicit scheme is straightforward and easy to implement, but the small time step due to the radiation diffusion term makes it computationally expensive. In [3, 7, 24], the authors implemented the implicit-explicit (IMEX) procedure where they treated the advection term explicitly and treated the nonlinear radiation diffusion term implicitly. The Newton iteration or the nonlinear generalized minimal residual (GMRES) methods for calculating the nonlinear implicit part in these high order IMEX Lagrangian schemes are computationally expensive and will consume a lot of computer memory, especially in the higher dimensional cases.

The explicit-implicit-null (EIN) method [23, 21] is a time-marching method which has been proven useful for solving problems with large time steps, where explicit methods may suffer from severe time step restrictions for stability imposed by the higher derivative terms. The EIN method combines the advantages of both explicit and implicit methods by adding a sufficiently large linear artificial high derivative term to both sides of the scheme and treating the linear artificial high derivative term on the right-hand side of the scheme implicitly, while the complex nonlinear terms are treated explicitly. When the coefficient of the added linear artificial high derivative term is chosen adequately, stability can be ensured with larger

time steps. By this treatment, we do not need a complicated nonlinear iterative solver. This method has been successfully applied to various problems in fluid dynamics, such as shock capturing and shock-turbulence interactions. Therefore, we design an EIN Lagrangian scheme in this paper to increase efficiency of our Lagrangian finite volume scheme for solving RHE.

In summary, we develop two types of high order, conservative schemes on the Lagrangian moving mesh. First, we will present the high order explicit Lagrangian scheme which preserves positivity well and is suitable for the advection-dominated RHE. Second, the EIN Lagrangian scheme is designed which can promote efficiency arising from the radiation diffusion term in the implementation. Supported by the high order multi-resolution WENO reconstruction for the spatial discretization, our Lagrangian schemes could achieve high order accuracy in smooth regions and capture shocks sharply without introducing oscillations. Furthermore, these Lagrangian schemes can automatically capture material interfaces, making them highly suitable for the multi-material problems where clear interfaces are essential.

The remainder of this paper is structured as follows. In Section 2, we analyze some properties of the two dimensional radiation hydrodynamics equations (RHE) in the equilibrium-diffusion limit. In Section 3, we introduce a high order explicit Lagrangian finite volume scheme for RHE and give the algorithm flowchart. In Section 4, we adopt a positivity-preserving limiter to preserve positivity for the above high order explicit Lagrangian scheme, without sacrificing the original high order accuracy. Next, in Section 5, we propose a high order EIN Lagrangian scheme. Then, several numerical tests are given to verify the performance of the two types of Lagrangian schemes in Section 6. Last, concluding remarks are given in Section 7.

2 Two-dimensional radiation hydrodynamics equations in the equilibrium-diffusion limit

We consider the following two-dimensional radiation hydrodynamics equations (RHE) in the equilibrium-diffusion limit [8],

$$\frac{\partial}{\partial t}\begin{pmatrix}\rho\\ \rho u\\ \rho v\\ E^*\end{pmatrix}+\frac{\partial}{\partial x}\begin{pmatrix}\rho u\\ \rho u^2+p^*\\ \rho uv\\ u(E^*+p^*)\end{pmatrix}+\frac{\partial}{\partial y}\begin{pmatrix}\rho v\\ \rho uv\\ \rho v^2+p^*\\ v(E^*+p^*)\end{pmatrix}=\frac{\partial}{\partial x}\begin{pmatrix}0\\ 0\\ 0\\ \kappa\partial_x T^4\end{pmatrix}+\frac{\partial}{\partial y}\begin{pmatrix}0\\ 0\\ 0\\ \kappa\partial_y T^4\end{pmatrix} \tag{2.1}$$

where u, v are velocities in the x, y directions, $E^* = E + E_r$, $p^* = p + p_r$ are the total energy and pressure of the system, respectively. $E_r = \mathcal{P}T^4$, $p_r = \frac{1}{3}\mathcal{P}T^4$ are the radiation energy and radiation pressure, where $\mathcal{P}$ is the radiation constant representing the radiation effects on the material dynamics. T is the temperature in the equilibrium-diffusion limit, where the matter and the radiation have the same temperature T. $\kappa = \frac{\mathcal{P}c}{3\sigma_t}$ is the diffusion coefficient, with the speed of light c and the total cross section σ_t.

The total pressure for the γ-law gas follows

$$p^* = (\gamma-1)\rho c_v T + \frac{1}{3}\mathcal{P}T^4,$$

where c_v is the heat capacity at constant volume, and the total energy follows

$$E^* = E + E_r = \rho c_v T + \frac{1}{2}\rho(u^2+v^2) + \mathcal{P}T^4.$$

So we have

$$T^4 + c_1 T + c_2 = 0, \quad c_1 := \frac{\rho c_v}{\mathcal{P}}, \quad c_2 := -\frac{1}{\mathcal{P}}\left(E^* - \frac{1}{2}\rho(u^2+v^2)\right), \tag{2.2}$$

and if $\mathcal{P} \le 10^{-6}$, we solve T from an asymptotic analysis,

$$T = \frac{E^* - \frac{1}{2}\rho(u^2+v^2)}{\rho c_v},$$

otherwise we will use the physically acceptable root of the quartic equation

$$T = \frac{1}{2}\left(-\sqrt{2s} + \sqrt{-2s + \frac{2c_1}{\sqrt{2s}}}\right), \quad \text{with} \quad s = \left[\frac{c_1^2}{16} + \sqrt{\frac{c_1^4}{256} - \frac{c_2^3}{27}}\right]^{\frac{1}{3}} - \left[-\frac{c_1^2}{16} + \sqrt{\frac{c_1^4}{256} - \frac{c_2^3}{27}}\right]^{\frac{1}{3}}.$$

We rewrite the radiation hydrodynamics equations (2.1) as

$$\partial_t \boldsymbol{U} + \partial_x \boldsymbol{F}_1(\boldsymbol{U}) + \partial_y \boldsymbol{F}_2(\boldsymbol{U}) = \partial_x \boldsymbol{G}_1(\boldsymbol{U}) + \partial_y \boldsymbol{G}_2(\boldsymbol{U}), \quad \boldsymbol{U} = \begin{pmatrix} \rho \\ \rho u \\ \rho v \\ E^* \end{pmatrix} \tag{2.3}$$

where

$$\boldsymbol{F}_1(\boldsymbol{U}) = \begin{pmatrix} \rho u \\ \rho u^2 + p^* \\ \rho uv \\ u(E^* + p^*) \end{pmatrix}, \ \boldsymbol{F}_2(\boldsymbol{U}) = \begin{pmatrix} \rho v \\ \rho uv \\ \rho v^2 + p^* \\ v(E^* + p^*) \end{pmatrix}, \ \boldsymbol{G}_1(\boldsymbol{U}) = \begin{pmatrix} 0 \\ 0 \\ 0 \\ \kappa \partial_x T^4 \end{pmatrix}, \ \boldsymbol{G}_2(\boldsymbol{U}) = \begin{pmatrix} 0 \\ 0 \\ 0 \\ \kappa \partial_y T^4 \end{pmatrix}.$$

Define the specific internal energy $e^* = \frac{E^*}{\rho} - \frac{u^2+v^2}{2}$, then the total pressure $p^* = p^*(\rho, e^*)$ which is a function of the density ρ and the internal energy e^*. The partial derivatives related to p^* are as follows

$$\begin{aligned}
\frac{\partial p^*}{\partial \rho} &= \left.\frac{\partial p^*}{\partial \rho}\right|_{e^*} + \left(\frac{u^2+v^2}{\rho} - \frac{E^*}{\rho^2}\right) \left.\frac{\partial p^*}{\partial e^*}\right|_{\rho} \\
\frac{\partial p^*}{\partial \rho u} &= -\frac{u}{\rho} \left.\frac{\partial p^*}{\partial e^*}\right|_{\rho}, \quad \frac{\partial p^*}{\partial \rho v} = -\frac{v}{\rho} \left.\frac{\partial p^*}{\partial e^*}\right|_{\rho}, \quad \frac{\partial p^*}{\partial E^*} = \frac{1}{\rho} \left.\frac{\partial p^*}{\partial e^*}\right|_{\rho} \\
\frac{\partial u p^*}{\partial \rho} &= u \left.\frac{\partial p^*}{\partial \rho}\right|_{e^*} + u \left(\frac{u^2+v^2}{\rho} - \frac{E^*}{\rho^2}\right) \left.\frac{\partial p^*}{\partial e^*}\right|_{\rho} - \frac{u}{\rho} p^* \\
\frac{\partial u p^*}{\partial \rho u} &= -\frac{u^2}{\rho} \left.\frac{\partial p^*}{\partial e^*}\right|_{\rho} + \frac{p^*}{\rho}, \quad \frac{\partial u p^*}{\partial \rho v} = -\frac{uv}{\rho} \left.\frac{\partial p^*}{\partial e^*}\right|_{\rho}, \quad \frac{\partial u p^*}{\partial E^*} = \frac{u}{\rho} \left.\frac{\partial p^*}{\partial e^*}\right|_{\rho}
\end{aligned} \tag{2.4}$$

with

$$q := \frac{1}{\rho} \left.\frac{\partial p^*}{\partial e^*}\right|_{\rho}, \ H := \frac{p^* + E^*}{\rho}, \ Q := \left.\frac{\partial p^*}{\partial \rho}\right|_{e^*} + \left(\frac{u^2+v^2}{\rho} - \frac{E^*}{\rho^2}\right) \left.\frac{\partial p^*}{\partial e^*}\right|_{\rho},$$

the acoustic speed $a^* := \sqrt{\left.\frac{\partial p^*}{\partial \rho}\right|_{e^*} + \frac{p^* \left.\frac{\partial p^*}{\partial e^*}\right|_{\rho}}{\rho^2}}$, and one can refer to [18] for more details.

Therefore, the Jacobian matrix follows as

$$\frac{\partial \boldsymbol{F}_1}{\partial \boldsymbol{U}} = \begin{pmatrix} 0 & 1 & 0 & 0 \\ Q - u^2 & u(2-q) & -vq & q \\ -uv & v & u & 0 \\ u(Q-H) & H - qu^2 & -quv & u(q+1) \end{pmatrix} \tag{2.5}$$

and the eigenvalues of $\frac{\partial \boldsymbol{F}_1}{\partial \boldsymbol{U}}$ are

$$\lambda^{(1)}_{\boldsymbol{F}_1} = u - a^*, \quad \lambda^{(2)}_{\boldsymbol{F}_1} = \lambda^{(3)}_{\boldsymbol{F}_1} = u, \quad \lambda^{(4)}_{\boldsymbol{F}_1} = u + a^*,$$

with the corresponding right eigenvectors

$$R^{(1)}_{\boldsymbol{F}_1}=\begin{pmatrix}1\\ u-a^*\\ v\\ H-ua^*\end{pmatrix},\quad R^{(2)}_{\boldsymbol{F}_1}=\begin{pmatrix}1\\ u\\ v\\ H-\frac{(a^*)^2}{q}\end{pmatrix},\quad R^{(3)}_{\boldsymbol{F}_1}=\begin{pmatrix}0\\ 0\\ 1\\ v\end{pmatrix},\quad R^{(4)}_{\boldsymbol{F}_1}=\begin{pmatrix}1\\ u+a^*\\ v\\ H+ua^*\end{pmatrix}$$

and its inverse matrix is

$$R^{-1}_{\boldsymbol{F}_1}=\frac{q}{2(a^*)^2}\begin{pmatrix}\frac{Q}{q}+\frac{ua^*}{q} & -u-\frac{a^*}{q} & -v & 1\\ 2H-2(u^2+v^2) & 2u & 2v & -2\\ -\frac{2v(a^*)^2}{q} & 0 & \frac{2(a^*)^2}{q} & 0\\ \frac{Q}{q}-\frac{ua^*}{q} & -u+\frac{a^*}{q} & -v & 1\end{pmatrix}. \tag{2.6}$$

On the other side, the Jacobian matrix of $\boldsymbol{F}_2(\boldsymbol{U})$ is

$$\frac{\partial \boldsymbol{F}_2}{\partial \boldsymbol{U}}=\begin{pmatrix}0 & 0 & 1 & 0\\ -uv & v & u & 0\\ Q-v^2 & -uq & v(2-q) & q\\ v(Q-H) & -quv & H-qv^2 & v(q+1)\end{pmatrix} \tag{2.7}$$

and the eigenvalues are

$$\lambda^{(1)}_{\boldsymbol{F}_2}=v-a^*,\quad \lambda^{(2)}_{\boldsymbol{F}_2}=\lambda^{(3)}_{\boldsymbol{F}_2}=v,\quad \lambda^{(4)}_{\boldsymbol{F}_2}=v+a^*,$$

with the corresponding right eigenvectors

$$R^{(1)}_{\boldsymbol{F}_2}=\begin{pmatrix}1\\ u\\ v-a^*\\ H-va^*\end{pmatrix},\quad R^{(2)}_{\boldsymbol{F}_2}=\begin{pmatrix}0\\ 1\\ 0\\ u\end{pmatrix},\quad R^{(3)}_{\boldsymbol{F}_2}=\begin{pmatrix}1\\ u\\ v\\ H-\frac{(a^*)^2}{q}\end{pmatrix},\quad R^{(4)}_{\boldsymbol{F}_2}=\begin{pmatrix}1\\ u\\ v+a^*\\ H+va^*\end{pmatrix}$$

and its inverse matrix is

$$R^{-1}_{\boldsymbol{F}_2}=\frac{q}{2(a^*)^2}\begin{pmatrix}\frac{Q}{q}+\frac{va^*}{q} & -u & -v-\frac{a^*}{q} & 1\\ -\frac{2u(a^*)^2}{q} & \frac{2(a^*)^2}{q} & 0 & 0\\ 2H-2(u^2+v^2) & 2u & 2v & -2\\ \frac{Q}{q}-\frac{va^*}{q} & -u & -v+\frac{a^*}{q} & 1\end{pmatrix}. \tag{2.8}$$

3 The explicit Lagrangian finite volume scheme for 2D RHE

In this section, we will introduce our cell-centered explicit Lagrangian finite volume scheme for the 2D radiation hydrodynamics equations in the equilibrium-diffusion limit (2.1).

3.1 High order spatial discretization

Consider the connected computational domain Ω consisting of quadrilateral cells $\{I_{i,j}\}_{i,j=1}^{N_x,N_y}$, where N_x and N_y are the number of cells in the x and y directions, respectively. Each cell $I_{i,j}$ has four nodes $P_{i-\frac{1}{2},j-\frac{1}{2}}$, $P_{i-\frac{1}{2},j+\frac{1}{2}}$, $P_{i+\frac{1}{2},j-\frac{1}{2}}$, $P_{i+\frac{1}{2},j+\frac{1}{2}}$ and the coordinate of $P_{i-\frac{1}{2},j-\frac{1}{2}}$ is $(x_{i-\frac{1}{2},j-\frac{1}{2}}, y_{i-\frac{1}{2},j-\frac{1}{2}})$, for all $1 \le i \le N_x,\ 1 \le j \le N_y$.

The 2D radiation hydrodynamics equations (2.3) in the reference frame of a moving control volume can be expressed in the integral form as

$$\frac{d}{dt}\int_{\Omega(t)} \boldsymbol{U} d\Omega + \int_{\Gamma(t)} \boldsymbol{F} d\Gamma = \int_{\Gamma(t)} \boldsymbol{G} d\Gamma \tag{3.9}$$

where $\Omega(t)$ is the moving control volume with boundary $\Gamma(t)$, and we take velocities of the control volume as fluid velocities, so we have

$$\boldsymbol{F}(\boldsymbol{U},\boldsymbol{n}) = \begin{pmatrix} 0 \\ n_x p^* \\ n_y p^* \\ p^*(u n_x + v n_y) \end{pmatrix}, \quad \boldsymbol{G}(\boldsymbol{U},\boldsymbol{n}) = \begin{pmatrix} 0 \\ 0 \\ 0 \\ \kappa(n_x \partial_x T^4 + n_y \partial_y T^4) \end{pmatrix} \tag{3.10}$$

and $\boldsymbol{n} = (n_x, n_y)^T$ is the outward unit normal vector of the boundary. Define the cell averages as

$$\begin{aligned} \bar{\rho}_{i,j} &= \frac{1}{|I_{i,j}|}\int_{I_{i,j}} \rho dxdy, \quad \bar{M}^x_{i,j} = \frac{1}{|I_{i,j}|}\int_{I_{i,j}} \rho u dxdy, \\ \bar{M}^y_{i,j} &= \frac{1}{|I_{i,j}|}\int_{I_{i,j}} \rho v dxdy, \quad \bar{E}^*_{i,j} = \frac{1}{|I_{i,j}|}\int_{I_{i,j}} E^* dxdy, \end{aligned}$$

then we have the following cell-centered semi-Lagrangian finite volume scheme

$$\begin{aligned} \frac{d}{dt}\begin{pmatrix} \bar{\rho}_{i,j}|I_{i,j}| \\ \bar{M}^x_{i,j}|I_{i,j}| \\ \bar{M}^y_{i,j}|I_{i,j}| \\ \bar{E}^*_{i,j}|I_{i,j}| \end{pmatrix} &= -\int_{\partial I_{i,j}} \widehat{\boldsymbol{F}} dl + \int_{\partial I_{i,j}} \widehat{\boldsymbol{G}} dl \\ &= -\int_{\partial I_{i,j}} \widehat{\boldsymbol{F}}(\boldsymbol{U}^{\text{in}}, \boldsymbol{U}^{\text{ex}}, \boldsymbol{n}) dl + \int_{\partial I_{i,j}} \widehat{\boldsymbol{G}}(\boldsymbol{U},\boldsymbol{n}) dl \end{aligned} \tag{3.11}$$

where the numerical fluxes are consistent with the physical flux (3.10), i.e.

$$\widehat{\boldsymbol{F}}(\boldsymbol{U},\boldsymbol{U},\boldsymbol{n}) = \boldsymbol{F}(\boldsymbol{U},\boldsymbol{n}) = (0, n_x p^*, n_y p^*, p^*(n_x u + n_y v))^T,$$

and

$$\widehat{\boldsymbol{G}}(\boldsymbol{U},\boldsymbol{n}) = \boldsymbol{G}(\boldsymbol{U},\boldsymbol{n}) = \left(0, 0, 0, \kappa(n_x \partial_x T^4, n_y \partial_y T^4)\right)^T.$$

Suppose that the cell $I_{i,j}$ has M edges (for our case $M = 4$) and the quadrature points on each edge are denoted as (x_α^m, y_α^m) for $m = 1, \cdots, M$, $\alpha = 1, \cdots, K$, where we omit the subscript i, j. Then we can write the line integral for the numerical flux as

$$\begin{aligned} \int_{\partial I_{i,j}} \widehat{\boldsymbol{F}} dl &\approx \sum_{m=1}^{M} |l^m| \sum_{\alpha=1}^{K} \omega_\alpha \widehat{\boldsymbol{F}} \left(\boldsymbol{U}^{\text{in}}(x_\alpha^m, y_\alpha^m), \boldsymbol{U}^{\text{ex}}(x_\alpha^m, y_\alpha^m), \boldsymbol{n}^m \right), \\ \int_{\partial I_{i,j}} \widehat{\boldsymbol{G}} dl &\approx \sum_{m=1}^{M} |l^m| \sum_{\alpha=1}^{K} \omega_\alpha \widehat{\boldsymbol{G}} \left(\boldsymbol{U}^{m}(x_\alpha^m, y_\alpha^m), \boldsymbol{n}^m \right), \end{aligned} \tag{3.12}$$

where ω_α, $\alpha = 1, \cdots, K$ are the weights in the quadrature rule, $|l^m|$ represents the length of the edge l^m for $m = 1, \cdots, M$ and $\boldsymbol{n}^m = (n_x^m, n_y^m)^T$ is the outward unit normal vector of l^m. $\boldsymbol{U}^{\text{in}}(x_\alpha^m, y_\alpha^m)$ and $\boldsymbol{U}^{\text{ex}}(x_\alpha^m, y_\alpha^m)$ are the values of the conserved variables on the cell $I_{i,j}$ and its neighboring cell along the edge l^m respectively. In fact, we use the Gauss-Lobatto quadrature rule, where (x_1^m, y_1^m) and (x_K^m, y_K^m) are the two endpoints of the edge l^m, and in this work we take $K = 3$. $\boldsymbol{U}^m(x_\alpha^m, y_\alpha^m)$ in the diffusion term are the values of the conserved variables on the common edge l^m.

We utilize the multi-resolution WENO reconstruction [28, 29] method to reconstruct high-order polynomials for the conserved variables. Particularly, for each cell $I_{i,j}$, we will reconstruct polynomials of different degrees on central nested stencils, then measure the smoothness of them and assign the corresponding nonlinear weights. Finally, we combine these polynomials with the nonlinear weights to get the high order polynomial

$$\boldsymbol{U}_{i,j}(x, y) = (\rho(x, y), M^x(x, y), M^y(x, y), E^*(x, y))_{i,j}^T.$$

In the smooth region, the combination of the polynomials can achieve high order accuracy, and near shocks or contact discontinuities, the combination will assign more weights on the low order polynomial to avoid numerical oscillation. Since we do not focus on the reconstruction here, we will leave the detailed description of the procedure to Appendix A.1. From the reconstruction polynomial $\boldsymbol{U}_{i,j}(x, y)$, we can obtain values of $\boldsymbol{U}^{\text{in}}(x_\alpha^m, y_\alpha^m)$ at each quadrature point for the numerical flux $\widehat{\boldsymbol{F}}$. Similarly, we can obtain $\boldsymbol{U}^{\text{ex}}(x_\alpha^m, y_\alpha^m)$ by the reconstruction polynomials in the neighboring cell.

We still follow the WENO idea to reconstruct high order polynomials $\boldsymbol{U}_{i,j}^m(x,y)$ on each edge l^m of the cell $I_{i,j}$ for the diffusion numerical flux $\widehat{\boldsymbol{G}}$, but the reconstruction strategy is different from that in the advection numerical flux $\widehat{\boldsymbol{F}}$. First, the values of the conserved variables and their derivatives are needed, so we should measure the smoothness of reconstruction polynomials starting from second order derivatives. Second, the reconstruction will be used to obtain the information on the edge l^m. For stability, the stencils for the reconstruction should include the cells at the both sides of l^m and should be conservative on them. We put the details of the reconstruction in Appendix A.2.

Then, we use the values of the conserved variables and their derivatives $\boldsymbol{U}_{i,j}^m(x_\alpha^m, y_\alpha^m)$, $\partial_x \boldsymbol{U}_{i,j}^m(x_\alpha^m, y_\alpha^m)$, $\partial_y \boldsymbol{U}_{i,j}^m(x_\alpha^m, y_\alpha^m)$ to calculate $\partial_x T^4(\boldsymbol{U}^m)$, $\partial_y T^4(\boldsymbol{U}^m)$ on the cell boundary l^m for the diffusion numerical flux,

$$\widehat{\boldsymbol{G}}(\boldsymbol{U}^m, \boldsymbol{n}^m) = (0, 0, 0, \kappa n_x^m \partial_x T^4(\boldsymbol{U}^m) + \kappa n_y^m \partial_y T^4(\boldsymbol{U}^m))^T.$$

Please see Appendix A.2 for the details.

The HLLC (Harten-Lax-van Leer contact wave) numerical flux [22, 6] is adopted for the advection numerical flux,

$$\widehat{\boldsymbol{F}}(\boldsymbol{U}^{\text{in}}, \boldsymbol{U}^{\text{ex}}, \boldsymbol{n}) = (0, n_x p^H, n_y p^H, p^H S^H)^T,$$

where p^H, S^H denote the pressure and velocity of the middle contact wave in the HLLC flux, respectively,

$$\begin{aligned} p^H &:= \rho^{\text{in}}(u_n^{\text{in}} - S_-)(u_n^{\text{in}} - S^H) + p^{*,\text{in}}, \\ S^H &:= \frac{\rho^{\text{ex}} u_n^{\text{ex}}(S_+ - u_n^{\text{ex}}) - \rho^{\text{in}} u_n^{\text{in}}(S_- - u_n^{\text{in}}) + p^{*,\text{in}} - p^{*,\text{ex}}}{\rho^{\text{ex}}(S_+ - u_n^{\text{ex}}) - \rho^{\text{in}}(S_- - u_n^{\text{in}})}, \end{aligned} \tag{3.13}$$

with

$$u_n^{\text{in}} = u^{\text{in}} n_x + v^{\text{in}} n_y, \quad u_n^{\text{ex}} = u^{\text{ex}} n_x + v^{\text{ex}} n_y,$$

and the left and right acoustic wavespeeds are

$$S_- = \min\{u_n^{\text{in}} - \frac{p^{*,\text{in}}}{\rho^{\text{in}}\sqrt{2e^{*,\text{in}}}}, u_n^{\text{in}} - a^{*,\text{in}}\}, \quad S_+ = \max\{u_n^{\text{ex}} + \frac{p^{*,\text{ex}}}{\rho^{\text{ex}}\sqrt{2e^{*,\text{ex}}}}, u_n^{\text{ex}} + a^{*,\text{ex}}\}. \tag{3.14}$$

In the Lagrangian finite volume scheme, we take the contact wave speed S^H as the velocity of the moving meshes.

Following [4, 6], for each edge connected to the vertex $P_{i+\frac{1}{2},j+\frac{1}{2}}$, we obtain the tangential velocities as an average on both sides, and obtain the normal velocities as S^H in the HLLC numerical flux. Finally, the velocity $(u_{i+\frac{1}{2},j+\frac{1}{2}}, v_{i+\frac{1}{2},j+\frac{1}{2}})$ at the vertex $P_{i+\frac{1}{2},j+\frac{1}{2}}$ is determined by computing the arithmetic average of the velocities along each edge.

3.2 High order time discretization

The first-order explicit Euler forward time discretization for the Lagrangian finite volume scheme follows as

$$\begin{aligned}
&\bar{\boldsymbol{U}}_{i,j}^{n+1}|I_{i,j}^{n+1}| - \bar{\boldsymbol{U}}_{i,j}^{n}|I_{i,j}| \\
=&\tau\left(-\int_{\partial I_{i,j}} \widehat{\boldsymbol{F}}^n dl + \int_{\partial I_{i,j}} \widehat{\boldsymbol{G}}^n dl\right) \\
=&-\tau\sum_{m=1}^{M}|l^m|\sum_{\alpha=1}^{K}\omega_\alpha \widehat{\boldsymbol{F}}\left(\boldsymbol{U}^{n,\text{in}}(x_\alpha^m, y_\alpha^m), \boldsymbol{U}^{n,\text{ex}}(x_\alpha^m, y_\alpha^m), \boldsymbol{n}^m\right) \\
&+\tau\sum_{m=1}^{M}|l^m|\sum_{\alpha=1}^{K}\omega_\alpha \widehat{\boldsymbol{G}}\left(\boldsymbol{U}^{n,m}(x_\alpha^m, y_\alpha^m), \boldsymbol{n}^m\right)
\end{aligned} \tag{3.15}$$

where $\bar{\boldsymbol{U}}_{i,j} = (\bar{\rho}_{i,j}, \bar{M}_{i,j}^x, \bar{M}_{i,j}^y, \bar{E}_{i,j}^*)^T$. We rewrite it as

$$\bar{\boldsymbol{U}}_{i,j}^{n+1}|I_{i,j}^{n+1}| - \bar{\boldsymbol{U}}_{i,j}^{n}|I_{i,j}^{n}| = \tau\mathbf{RHS}(\bar{\boldsymbol{U}}_{i,j}^{n}), \quad \mathbf{RHS}(\bar{\boldsymbol{U}}_{i,j}^{n}) := -\int_{\partial I_{i,j}^n} \widehat{\boldsymbol{F}}^n dl + \int_{\partial I_{i,j}^n} \widehat{\boldsymbol{G}}^n dl, \tag{3.16}$$

where $\mathbf{RHS}(\bar{\boldsymbol{U}}_{i,j}^{n})$ is the spatial discretization operator.

Actually, we implement the third order strong stability-preserving Runge-Kutta (SSP-RK) [9] time discretization for the explicit Lagrangian scheme in the following way

- Step 1.

$$\begin{aligned}
x_{i+\frac{1}{2},j+\frac{1}{2}}^{(1)} &= x_{i+\frac{1}{2},j+\frac{1}{2}}^{n} + \tau u_{i+\frac{1}{2},j+\frac{1}{2}}^{n}, \\
y_{i+\frac{1}{2},j+\frac{1}{2}}^{(1)} &= y_{i+\frac{1}{2},j+\frac{1}{2}}^{n} + \tau v_{i+\frac{1}{2},j+\frac{1}{2}}^{n}, \\
\bar{\boldsymbol{U}}_{i,j}^{(1)}|I_{i,j}^{(1)}| &= \bar{\boldsymbol{U}}_{i,j}^{n}|I_{i,j}^{n}| + \tau\mathbf{RHS}(\bar{\boldsymbol{U}}_{i,j}^{n})
\end{aligned} \tag{3.17}$$

- Step 2.

$$\begin{aligned} x^{(2)}_{i+\frac{1}{2},j+\frac{1}{2}} &= \frac{3}{4}x^{n}_{i+\frac{1}{2},j+\frac{1}{2}} + \frac{1}{4}\left(x^{(1)}_{i+\frac{1}{2},j+\frac{1}{2}} + \tau u^{(1)}_{i+\frac{1}{2},j+\frac{1}{2}}\right), \\ y^{(2)}_{i+\frac{1}{2},j+\frac{1}{2}} &= \frac{3}{4}y^{n}_{i+\frac{1}{2},j+\frac{1}{2}} + \frac{1}{4}\left(y^{(1)}_{i+\frac{1}{2},j+\frac{1}{2}} + \tau v^{(1)}_{i+\frac{1}{2},j+\frac{1}{2}}\right), \\ \bar{\boldsymbol{U}}^{(2)}_{i,j}|I^{(2)}_{i,j}| &= \frac{3}{4}\bar{\boldsymbol{U}}^{n}_{i,j}|I^{n}_{i,j}| + \frac{1}{4}\left(\bar{\boldsymbol{U}}^{(1)}_{i,j}|I^{(1)}_{i,j}| + \tau\mathbf{RHS}(\bar{\boldsymbol{U}}^{(1)}_{i,j})\right) \end{aligned} \tag{3.18}$$

- Step 3.

$$\begin{aligned} x^{n+1}_{i+\frac{1}{2},j+\frac{1}{2}} &= \frac{1}{3}x^{n}_{i+\frac{1}{2},j+\frac{1}{2}} + \frac{2}{3}\left(x^{(2)}_{i+\frac{1}{2},j+\frac{1}{2}} + \tau u^{(2)}_{i+\frac{1}{2},j+\frac{1}{2}}\right), \\ y^{n+1}_{i+\frac{1}{2},j+\frac{1}{2}} &= \frac{1}{3}y^{n}_{i+\frac{1}{2},j+\frac{1}{2}} + \frac{2}{3}\left(y^{(2)}_{i+\frac{1}{2},j+\frac{1}{2}} + \tau v^{(2)}_{i+\frac{1}{2},j+\frac{1}{2}}\right), \\ \bar{\boldsymbol{U}}^{n+1}_{i,j}|I^{n+1}_{i,j}| &= \frac{1}{3}\bar{\boldsymbol{U}}^{n}_{i,j}|I^{n}_{i,j}| + \frac{2}{3}\left(\bar{\boldsymbol{U}}^{(2)}_{i,j}|I^{(2)}_{i,j}| + \tau\mathbf{RHS}(\bar{\boldsymbol{U}}^{(2)}_{i,j})\right) \end{aligned} \tag{3.19}$$

Therefore, our explicit Lagrangian finite volume scheme is high order accurate in space and time and we will verify this in the later experiments.

3.3 Time step constraints

Denote τ^n as the time step at time $t = t^n$, which is determined by the limitation of the time step conditions arising from the advection term τ^n_{ad}, the diffusion term τ^n_{diff} and the mesh constraint τ^n_{mesh}, respectively,

$$\tau^n = \min\left\{\tau^n_{ad},\ \tau^n_{diff},\ \tau^n_{mesh}\right\}.$$

First, the time step should satisfy the CFL condition,

$$\tau^n \le \tau^n_{ad} := \lambda \min_{i,j} \frac{h^n_{i,j}}{\bar{a}^{*,n}_{i,j}}, \tag{3.20}$$

where $h^n_{i,j}$ is the circumscribed circle diameter of the cell $I_{i,j}$. Then, due to the existence of the diffusion term, the time step should satisfy the following limitation derived from the Fourier stability analysis

$$\tau^n \le \tau^n_{diff} := \mu \min_{i,j}(h^n_{i,j})^2 \frac{c_v\bar{\rho}^n_{i,j} + 4\mathcal{P}(\bar{T}^n_{i,j})^3}{4\kappa(\bar{T}^n_{i,j})^3\sqrt{1 + (\bar{u}^n_{i,j})^2 + (\bar{v}^n_{i,j})^2 + \left(\frac{(\bar{u}^n_{i,j})^2+(\bar{v}^n_{i,j})^2}{2} - c_v\bar{T}^n_{i,j}\right)^2}}. \tag{3.21}$$

Finally, to avoid the mesh being twisted, we require that

$$\tau^n \le \tau^n_{mesh} := \xi \min_{i,j} \left\{ \frac{|P_{i-\frac{1}{2},j-\frac{1}{2}} - P_{i+\frac{1}{2},j-\frac{1}{2}}|}{w^n_{i-\frac{1}{2},j-\frac{1}{2}}}, \frac{|P_{i-\frac{1}{2},j-\frac{1}{2}} - P_{i-\frac{1}{2},j+\frac{1}{2}}|}{w^n_{i-\frac{1}{2},j-\frac{1}{2}}}, \frac{|P_{i-\frac{1}{2},j-\frac{1}{2}} - P_{i-\frac{3}{2},j-\frac{1}{2}}|}{w^n_{i-\frac{1}{2},j-\frac{1}{2}}}, \frac{|P_{i-\frac{1}{2},j-\frac{1}{2}} - P_{i-\frac{1}{2},j-\frac{3}{2}}|}{w^n_{i-\frac{1}{2},j-\frac{1}{2}}} \right\}, \tag{3.22}$$

where $w^n_{i-\frac{1}{2},j-\frac{1}{2}} := \sqrt{\left(u^n_{i-\frac{1}{2},j-\frac{1}{2}}\right)^2 + \left(v^n_{i-\frac{1}{2},j-\frac{1}{2}}\right)^2}$, and $|P_{i-\frac{1}{2},j-\frac{1}{2}} - P_{i+\frac{1}{2},j-\frac{1}{2}}|$ measures the distance between $P_{i-\frac{1}{2},j-\frac{1}{2}}$ and $P_{i+\frac{1}{2},j-\frac{1}{2}}$.

λ, ξ, μ are constants in $[0, 1]$, specifically, we take $\lambda = \xi = 0.5$, $\mu = 0.25$. The time scale of the fluid advection $\tau^n_{ad} = \mathcal{O}(h)$ is usually larger than that of the radiation diffusion $\tau^n_{diff} = \mathcal{O}(\frac{h^2}{\kappa})$, so the time step condition τ is usually dominated by τ^n_{diff}, especially when the parameter κ is not very small.

3.4 Flow chart of the explicit Lagrangian finite volume scheme

Now, we give the flow chart of the explicit Lagrangian finite volume scheme with the Euler forward time discretization as an example. Suppose we have known the cell averages $\bar{\boldsymbol{U}}^n_{i,j}$ for all the cells at time level $t = t^n$, then we want to get the new cell averages $\bar{\boldsymbol{U}}^{n+1}_{i,j}$ at the next time level $t = t^{n+1}$.

1. For the determination of the advection term $\widehat{\boldsymbol{F}}$, reconstruct high order polynomials with the cell averages $\bar{\boldsymbol{U}}^n_{i,j}$,

   $$\boldsymbol{U}^n_{i,j}(x, y) = (\rho(x, y), M^x(x, y), M^y(x, y), E^*(x, y))^{n,T}_{i,j}$$

   over each cell $I_{i,j}$ employing multi-resolution WENO reconstruction. The details of the WENO reconstruction are listed in Appendix A.1.

2. Calculate the values at the quadrature points on the cell boundaries $\boldsymbol{U}^{\text{in}}_{i,j}(x^m_\alpha, y^m_\alpha)$, $\boldsymbol{U}^{\text{ex}}_{i,j}(x^m_\alpha, y^m_\alpha)$ at time level $t = t^n$ for $\int_{\partial I_{i,j}} \widehat{\boldsymbol{F}}(\boldsymbol{U}^{\text{in}}, \boldsymbol{U}^{\text{ex}}, \boldsymbol{n}) dl$.

3. For the determination of the diffusion term $\widehat{\boldsymbol{G}}$, reconstruct high order polynomials with the cell averages $\bar{\boldsymbol{U}}_{i,j}^n$,

$$\boldsymbol{U}_{i,j}^{n,m}(x,y) = (\rho(x,y), M^x(x,y), M^y(x,y), E^*(x,y))_{i,j}^{n,m,T}$$

over each edge l^m of the cell $I_{i,j}$ by the multi-resolution WENO reconstruction again. One can refer to Appendix A.2 for the details.

4. Calculate the values and derivatives of the conserved variables

$$\boldsymbol{U}_{i,j}^{n,m}(x_\alpha^m, y_\alpha^m), \quad \partial_x \boldsymbol{U}_{i,j}^{n,m}(x_\alpha^m, y_\alpha^m), \quad \partial_y \boldsymbol{U}_{i,j}^{n,m}(x_\alpha^m, y_\alpha^m)$$

at the quadrature points on the cell boundaries. Then, calculate $\partial_x T^4(\boldsymbol{U}^{n,m})$, $\partial_y T^4(\boldsymbol{U}^{n,m})$ at the time level $t = t^n$ in the diffusion numerical flux $\int_{\partial I_{i,j}} \widehat{\boldsymbol{G}}(\boldsymbol{U}^m, \boldsymbol{n}^m) dl$.

5. Update the new mesh by

$$x_{i+\frac{1}{2},j+\frac{1}{2}}^{n+1} = x_{i+\frac{1}{2},j+\frac{1}{2}}^n + \tau u_{i+\frac{1}{2},j+\frac{1}{2}}^n, \quad y_{i+\frac{1}{2},j+\frac{1}{2}}^{n+1} = y_{i+\frac{1}{2},j+\frac{1}{2}}^n + \tau v_{i+\frac{1}{2},j+\frac{1}{2}}^n,$$

where $0 \le i \le N_x,\ 0 \le j \le N_y$ and $u_{i+\frac{1}{2},j+\frac{1}{2}}^n, v_{i+\frac{1}{2},j+\frac{1}{2}}^n$ are the nodal velocities.

6. Calculate the new cell averages at the next time level $t = t^{n+1}$ with the Euler forward time discretization (3.16),

$$\bar{\boldsymbol{U}}_{i,j}^{n+1} = \frac{|I_{i,j}^n|}{|I_{i,j}^{n+1}|} \bar{\boldsymbol{U}}_{i,j}^n + \frac{\tau}{|I_{i,j}^{n+1}|} \mathbf{RHS}(\bar{\boldsymbol{U}}_{i,j}^n).$$

Although the above flowchart is designed for the first-order Euler forward time discretization, it is easy to extend to high-order SSP-RK time discretization which is the convex combination of the Euler forward method, by repeating the above procedure several times.

4 The positivity-preserving explicit Lagrangian scheme

As we know, some physical variables in RHE such as density, internal energy and temperature should be positive, so we hope our numerical schemes could preserve positivity well for

them. Specifically, in the finite volume method, we hope the cell averages $\bar{\rho}^{n+1}, \bar{e}^{*,n+1}, \bar{T}^{n+1}$ calculated by the explicit scheme are positive, if the inputs $\bar{\rho}^{n}, \bar{e}^{*,n}, \bar{T}^{n}$ are positive.

Before discussing the positivity-preserving property of the schemes, we first extend the two lemmas given in [7] to the two-dimensional RHE. The proof is similar, so we skip it here.

Lemma 4.1. *If* $\rho > 0$ *then* $T > 0 \quad \Leftrightarrow \quad e^* > 0$

Lemma 4.2. *The set of admissible states* $G := \left\{ \boldsymbol{U} = \begin{pmatrix} \rho \\ \rho u \\ \rho v \\ E^* \end{pmatrix}, \ \rho > 0, \ e^* > 0 \right\}$ *is convex.*

Later, we will prove that if the input $\bar{\boldsymbol{U}}^n \in G$, the new cell averages are also in the admissible set $\bar{\boldsymbol{U}}^{n+1} \in G$, which means the new cell averages $\bar{\rho}^{n+1}, \bar{e}^{*,n+1}, \bar{T}^{n+1}$ are positive.

4.1 The first order positivity-preserving explicit Lagrangian scheme

Let us start from the first order explicit scheme, then we will extend these results to the high order case. For the first order scheme, the reconstruction polynomials are constants for the advection terms $\boldsymbol{U}_{i,j}(x,y) = \bar{\boldsymbol{U}}_{i,j}$ and the polynomials for the diffusion terms are linear, denoted as $\boldsymbol{U}^m_{i,j}(x,y) = \boldsymbol{U}^m_{i,j,lin}(x,y)$, since the first order derivatives are involved. Use the middle-point integration formula for the line integrals $\int_{\partial I} \widehat{\boldsymbol{F}} dl$, $\int_{\partial I} \widehat{\boldsymbol{G}} dl$, so the first order scheme (3.15) becomes

$$\begin{aligned} \bar{\boldsymbol{U}}^{n+1}|I^{n+1}| =& \frac{1}{2}\bar{\boldsymbol{U}}^{n}|I^{n}| - \tau \sum_{m=1}^{M} |l^m| \widehat{\boldsymbol{F}}\left(\bar{\boldsymbol{U}}^{n}, \bar{\boldsymbol{U}}^{n,\mathrm{ex}(l^m)}, \boldsymbol{n}^m\right) \\ &+ \frac{1}{2}\bar{\boldsymbol{U}}^{n}|I^{n}| + \tau \sum_{m=1}^{M} |l^m| \widehat{\boldsymbol{G}}\left(\boldsymbol{U}^{n,m}_{lin}(x^m_c, y^m_c), \boldsymbol{n}^m\right) \\ =& \frac{1}{2}W_1 + \frac{1}{2}W_2 \end{aligned} \tag{4.23}$$

where we omit the cell index i, j in this subsection to be more concise, $\bar{\boldsymbol{U}}^{n,\mathrm{ex}(l^m)}$ represents the cell averages on the other side of the edge l^m, (x^m_c, y^m_c) is the middle point of l^m, and

W_1, W_2 are defined as

$$W_1 = \begin{pmatrix} \bar{\rho}_1|I^{n+1}| \\ \bar{M}_1^x|I^{n+1}| \\ \bar{M}_1^y|I^{n+1}| \\ \bar{E}_1^*|I^{n+1}| \end{pmatrix} := \bar{\boldsymbol{U}}^n|I^n| - 2\tau \sum_{m=1}^{M} |l^m| \widehat{\boldsymbol{F}}\left(\bar{\boldsymbol{U}}^n, \bar{\boldsymbol{U}}^{n,\mathrm{ex}(l^m)}, \boldsymbol{n}^m\right)$$

$$W_2 = \begin{pmatrix} \bar{\rho}_2|I^{n+1}| \\ \bar{M}_2^x|I^{n+1}| \\ \bar{M}_2^y|I^{n+1}| \\ \bar{E}_2^*|I^{n+1}| \end{pmatrix} := \bar{\boldsymbol{U}}^n|I^n| + 2\tau \sum_{m=1}^{M} |l^m| \widehat{\boldsymbol{G}}\left(\boldsymbol{U}_{lin}^{n,m}(x_c^m, y_c^m), \boldsymbol{n}^m\right)$$

Next, we will prove that if we know cell averages $\bar{\boldsymbol{U}}^n \in G$, then we have $W_1, W_2 \in G$ under the suitable time step conditions, furthermore $\bar{\boldsymbol{U}}^{n+1} = \frac{W_1}{2|I^{n+1}|} + \frac{W_2}{2|I^{n+1}|} \in G$, since G is convex.

For any closed cell I^n, we have $\sum_{m=1}^{M} \boldsymbol{n}^m |l^m| = \boldsymbol{0}$, and $\widehat{\boldsymbol{F}}(\bar{\boldsymbol{U}}^n, \bar{\boldsymbol{U}}^n, \boldsymbol{n}^m) = \boldsymbol{F}(\bar{\boldsymbol{U}}^n, \boldsymbol{n}^m)$ due to the consistency of the numerical flux. Then, we have

$$\begin{aligned} \sum_{m=1}^{M} \widehat{\boldsymbol{F}}(\bar{\boldsymbol{U}}^n, \bar{\boldsymbol{U}}^n, \boldsymbol{n}^m)|l^m| &= \sum_{m=1}^{M} \boldsymbol{F}(\bar{\boldsymbol{U}}^n, \boldsymbol{n}^m)|l^m| \\ &= \begin{pmatrix} 0 \\ \bar{p}^{*,n} \sum_{m=1}^{M} n_x^m |l^m| \\ \bar{p}^{*,n} \sum_{m=1}^{M} n_y^m |l^m| \\ \bar{p}^{*,n} (\bar{u}^n \sum_{m=1}^{M} n_x^m |l^m| + \bar{v}^n \sum_{m=1}^{M} n_y^m |l^m|) \end{pmatrix} = \boldsymbol{0} \end{aligned} \tag{4.24}$$

and add this item in W_1,

$$\begin{aligned} W_1 = &\ \bar{\boldsymbol{U}}^n|I^n| - 2\tau \sum_{m=1}^{M} |l^m| \left[\widehat{\boldsymbol{F}}\left(\bar{\boldsymbol{U}}^n, \bar{\boldsymbol{U}}^{n,\mathrm{ex}(l^m)}, \boldsymbol{n}^m\right) - \widehat{\boldsymbol{F}}(\bar{\boldsymbol{U}}^n, \bar{\boldsymbol{U}}^n, \boldsymbol{n}^m)\right] \\ = &\ \sum_{m=1}^{M} |l^m| \left[\frac{|I^n|}{\sum_{m=1}^{M} |l^m|} |\bar{\boldsymbol{U}}^n| - 2\tau \left(\widehat{\boldsymbol{F}}\left(\bar{\boldsymbol{U}}^n, \bar{\boldsymbol{U}}^{n,\mathrm{ex}(l^m)}, \boldsymbol{n}^m\right) - \widehat{\boldsymbol{F}}(\bar{\boldsymbol{U}}^n, \bar{\boldsymbol{U}}^n, \boldsymbol{n}^m)\right)\right]. \end{aligned} \tag{4.25}$$

This is similar to the one-dimensional case, namely the same type as (5.8) in [7]. Thus, if the acoustic wavespeeds in the HLLC flux satisfy (3.14), then under the following CFL condition, we have $W_1 \in G$,

$$\tau \le \frac{\lambda}{2} \min_{i,j} \left(\frac{|I_{i,j}^n|}{\sum_{m=1}^{M} |l_{i,j}^m|} \Big/ \max\left\{ \left| \frac{\bar{p}_{i,j}^{*,n}}{\bar{\rho}_{i,j}^n \sqrt{2\bar{e}_{i,j}^{*,n}}} \right|, \bar{a}_{i,j}^{*,n} \right\} \right) \tag{4.26}$$

with $\lambda = 0.5$.

For the second part W_2, the density $\bar{\rho}_2 = \bar{\rho}^n$ must be positive if $\bar{\rho}^n > 0$. Let us consider the internal energy

$$\begin{aligned}
\bar{e}_2^* = &\ \bar{E}_2^* - \frac{1}{2}\frac{(\bar{M}_2^x)^2 + (\bar{M}_2^y)^2}{\bar{\rho}_2} \\
= &\ \bar{E}^{*,n} + 2\tau \sum_{m=1}^{M} \frac{|l^m|}{|I^n|} \left(\hat{g}(\boldsymbol{U}_{lin}^{n,m}(x_c^m, y_c^m), \boldsymbol{n}^m)\right) - \frac{(\bar{M}^{x,n})^2 + (\bar{M}^{y,n})^2}{2\bar{\rho}^n} \\
= &\ \bar{e}^{*,n} + 2\tau \sum_{m=1}^{M} \frac{|l^m|}{|I^n|} \left(\hat{g}(\boldsymbol{U}_{lin}^{n,m}(x_c^m, y_c^m), \boldsymbol{n}^m)\right) \\
= &\ \sum_{m=1}^{M} \frac{|l^m|}{|I^n|} \left[\frac{|I^n|}{\sum_{m=1}^{M} |l^m|} \bar{e}^{*,n} + 2\tau \hat{g}(\boldsymbol{U}_{lin}^{n,m}(x_c^m, y_c^m), \boldsymbol{n}^m)\right]
\end{aligned}$$

where $\hat{g}(\boldsymbol{U}_{lin}^{n,m}(x_c^m, y_c^m), \boldsymbol{n}^m) := \kappa n_x^m \partial_x T^4(\boldsymbol{U}_{lin}^{n,m}(x_c^m, y_c^m)) + \kappa n_y^m \partial_y T^4(\boldsymbol{U}_{lin}^{n,m}(x_c^m, y_c^m))$, and $T(\boldsymbol{U}_{lin}^{n,m}(x_c^m, y_c^m))$ represents the temperature calculated by the conserved variables $\boldsymbol{U}_{lin}^{n,m}(x_c^m, y_c^m)$. Then, we have the conclusion that $\bar{e}_2^* > 0$ and $W_2 \in G$, if

$$\tau \leq \frac{\lambda}{2\kappa} \min_{i,j} \left(\frac{|I_{i,j}^n|}{\sum_{m=1}^{M} |l_{i,j}^m|} \cdot \frac{\bar{e}_{i,j}^{*,n}}{\varepsilon + \sqrt{2} \max_m \{|\partial_x T^4(\boldsymbol{U}_{i,j,lin}^{n,m}(x_c^m, y_c^m))|, |\partial_y T^4(\boldsymbol{U}_{i,j,lin}^{n,m}(x_c^m, y_c^m))|\}} \right) \tag{4.27}$$

where $\lambda = 0.5$, $\varepsilon = 10^{-13}$ is a small positive constant to avoid zero in denominator. By using the fact the admissible set G is convex, we have the following theorem.

Theorem 4.1. *Consider the first-order explicit Lagrangian finite volume method (3.15) solving (2.1) with the HLLC numerical flux. If the cell averages $\bar{\boldsymbol{U}}_{i,j}^n \in G$ for all of the cells $I_{i,j}$ at the time level $t = t^n$, then the new cell averages $\bar{\boldsymbol{U}}_{i,j}^{n+1} \in G$ preserving positivity under the time step constraints (4.26) and (4.27).*

4.2 The high order positivity-preserving explicit Lagrangian scheme

Now, let us move forward to the high order scheme. In the FVM framework with the first-order Euler forward method, the new cell averages $\bar{\boldsymbol{U}}_{i,j}^{n+1}$ at the time level $t = t^{n+1}$ are calculated via (3.15) with the high order reconstruction polynomial $\boldsymbol{U}_{i,j}^n(x, y)$. Now, we will prove that, if the values $\boldsymbol{U}_{i,j}^n(x_{\alpha,\beta}, y_{\alpha,\beta})$ obtained from $\boldsymbol{U}_{i,j}^n(x, y)$ at the quadrature points satisfy $\boldsymbol{U}_{i,j}^n(x_{\alpha,\beta}, y_{\alpha,\beta}) \in G$, then we have $\bar{\boldsymbol{U}}_{i,j}^{n+1} \in G$ with suitable time step conditions. In

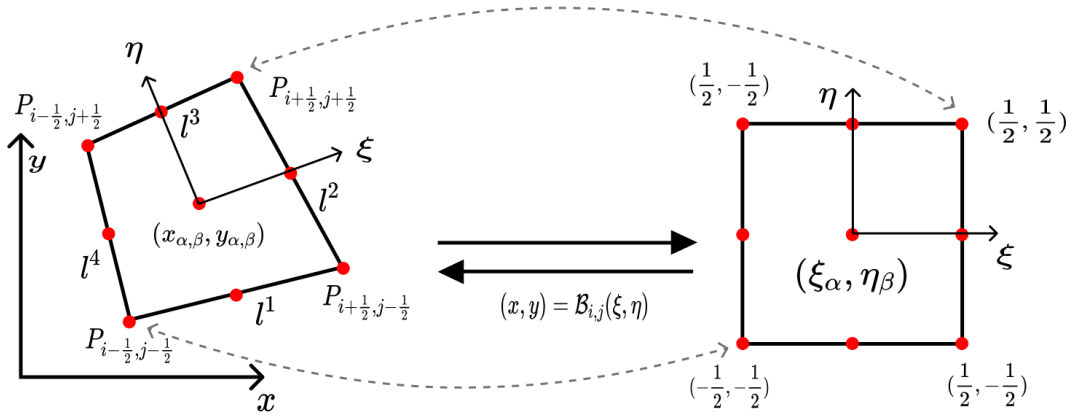

Figure 4.1: Transformation between the physical cell $I_{i,j}$ and the reference cell I_0.

the meantime, the high-order SSP-RK scheme is the convex combination of the first Euler forward scheme, so this conclusion can be extended to the high order scheme in time.

Just like before, we omit the cell index i, j to make the proof more concise. In this subsection, we use the Gauss-Lobatto quadrature rule for the integral and convert the physical cell $I_{i,j}$ to the reference cell $I_0 = [-\frac{1}{2}, \frac{1}{2}] \times [-\frac{1}{2}, \frac{1}{2}]$, in the ξ-η coordinates, see Figure 4.1 for the details. Let us consider the case that the degree of our reconstruction polynomials are at most third order, we can use the 3×3 points tensor product Simpson quadrature rule with $\omega_1 = \frac{1}{6}, \omega_2 = \frac{2}{3}, \omega_3 = \frac{1}{6}$. If the polynomial degree is higher, we may need to use a higher order tensor product Gauss-Lobatto rule. For the nine quadrature points (ξ_α, η_β) in I_0, we have the bilinear mapping $\mathcal{B}_{i,j}(\xi, \eta)$ to the quadrature points $(x_{\alpha,\beta}, y_{\alpha,\beta}) = \mathcal{B}_{i,j}(\xi_\alpha, \eta_\beta)$ on the physical cell $I_{i,j}$ with $1 \le \alpha, \beta \le 3$. We note that points $(x_{\alpha,1}, y_{\alpha,1})$ are on the edge l^1, points $(x_{K,\beta}, y_{K,\beta})$ are on the edge l^2, points $(x_{\alpha,K}, y_{\alpha,K})$ are on the edge l^3 and points $(x_{1,\beta}, y_{1,\beta})$ are on the edge l^4. It is worth mentioning that, since we use the Gauss-Lobatto quadrature rule for the line integral, and the two-dimensional quadrature rule is the tensor product of the ξ, η directions, the quadrature points on each edge l^m in (3.15) are also the quadrature points in (4.28). Specifically, we have $(x_{\alpha,1}, y_{\alpha,1}) \Leftrightarrow (x_\alpha^1, y_\alpha^1)$ on the edge l^1, $(x_{K,\beta}, y_{K,\beta}) \Leftrightarrow (x_{K,\alpha}, y_{K,\alpha}) \Leftrightarrow (x_\alpha^2, y_\alpha^2)$ on the edge l^2, $(x_{\alpha,K}, y_{\alpha,K}) \Leftrightarrow (x_\alpha^3, y_\alpha^3)$ on the edge l^3 and $(x_{1,\beta}, y_{1,\beta}) \Leftrightarrow (x_{1,\alpha}, y_{1,\alpha}) \Leftrightarrow (x_\alpha^4, y_\alpha^4)$ on the edge l^4.

Therefore, the integral over $I_{i,j}$ can be written as

$$\begin{aligned} |I^n|\bar{\boldsymbol{U}}^n = & \iint_I \boldsymbol{U}(x,y)dxdy \\ = & \iint_{I_0} \boldsymbol{U}(\mathcal{B}(\xi,\eta)) \left|\frac{\partial \mathcal{B}}{\partial(\xi,\eta)}\right| d\xi d\eta \\ = & \sum_{\alpha=1}^{K}\sum_{\beta=1}^{K} \omega_\alpha\omega_\beta \left|\frac{\partial \mathcal{B}}{\partial(\xi,\eta)}\right|_{(\xi_\alpha,\eta_\beta)} \boldsymbol{U}^{\alpha,\beta} \\ = & \sum_{\alpha=1}^{K}\sum_{\beta=1}^{K} \tilde{\omega}_{\alpha,\beta}\boldsymbol{U}^{\alpha,\beta}|J|^{\alpha,\beta} \end{aligned} \tag{4.28}$$

where $\left|\frac{\partial \mathcal{B}}{\partial(\xi,\eta)}\right|$ is the Jacobian matrix of the coordinate transformation, and we denote $\boldsymbol{U}^{\alpha,\beta} := \boldsymbol{U}(\mathcal{B}(\xi_\alpha,\eta_\beta)) = \boldsymbol{U}(x_{\alpha,\beta},y_{\alpha,\beta})$, $\tilde{\omega}_{\alpha,\beta} := \omega_\alpha\omega_\beta$ and $|J|^{\alpha,\beta} := \left|\frac{\partial \mathcal{B}}{\partial(\xi,\eta)}\right|_{(\xi_\alpha,\eta_\beta)}$. Separate the integral (4.28) as

$$\begin{aligned} |I^n|\bar{\boldsymbol{U}}^n = & \frac{1}{2}|I^n|\bar{\boldsymbol{U}}^n + \frac{1}{2}|I^n|\bar{\boldsymbol{U}}^n \\ = & \frac{1}{2}\left[\sum_{\alpha=1}^{K}\tilde{\omega}_{\alpha,1}\boldsymbol{U}^{\alpha,1}|J|^{\alpha,1} + \sum_{\alpha=1}^{K}\tilde{\omega}_{\alpha,K}\boldsymbol{U}^{\alpha,K}|J|^{\alpha,K} + \sum_{\alpha=1}^{K}\sum_{\beta=2}^{K-1}\tilde{\omega}_{\alpha,\beta}\boldsymbol{U}^{\alpha,\beta}|J|^{\alpha,\beta}\right] \\ & + \frac{1}{2}\left[\sum_{\alpha=1}^{K}\tilde{\omega}_{1,\alpha}\boldsymbol{U}^{1,\alpha}|J|^{1,\alpha} + \sum_{\alpha=1}^{K}\tilde{\omega}_{K,\alpha}\boldsymbol{U}^{K,\alpha}|J|^{K,\alpha} + \sum_{\alpha=2}^{K-1}\sum_{\beta=1}^{K}\tilde{\omega}_{\alpha,\beta}\boldsymbol{U}^{\alpha,\beta}|J|^{\alpha,\beta}\right] \\ = & \frac{1}{2}\left[\sum_{\alpha=1}^{K}\sum_{\beta=2}^{K-1}\tilde{\omega}_{\alpha,\beta}\boldsymbol{U}^{\alpha,\beta}|J|^{\alpha,\beta} + \sum_{\alpha=2}^{K-1}\sum_{\beta=1}^{K}\tilde{\omega}_{\alpha,\beta}\boldsymbol{U}^{\alpha,\beta}|J|^{\alpha,\beta}\right] \\ & + \frac{1}{2}\omega_1\sum_{\alpha=1}^{K}\omega_\alpha\left(\boldsymbol{U}^{\alpha,1}|J|^{\alpha,1} + \boldsymbol{U}^{1,\alpha}|J|^{1,\alpha} + \boldsymbol{U}^{\alpha,K}|J|^{\alpha,K} + \boldsymbol{U}^{K,\alpha}|J|^{K,\alpha}\right). \end{aligned} \tag{4.29}$$

Consider the first order Euler forward discretization (3.15) with high order reconstruction polynomials

$$\begin{aligned} & \bar{\boldsymbol{U}}^{n+1}|I^{n+1}| \\ = & \frac{1}{2}\bar{\boldsymbol{U}}^n|I^n| - \tau\sum_{m=1}^{M}|l^m|\sum_{\alpha=1}^{K}\omega_\alpha\widehat{\boldsymbol{F}}\left(\boldsymbol{U}^{\text{in}}(x_\alpha^m,y_\alpha^m),\boldsymbol{U}^{\text{ex}}(x_\alpha^m,y_\alpha^m),\boldsymbol{n}^m\right) \\ & + \frac{1}{2}\bar{\boldsymbol{U}}^n|I^n| + \tau\sum_{m=1}^{M}|l^m|\sum_{\alpha=1}^{K}\omega_\alpha\widehat{\boldsymbol{G}}\left(\boldsymbol{U}^m(x_\alpha^m,y_\alpha^m),\boldsymbol{n}^m\right) \\ = & \frac{1}{2}W_1 + \frac{1}{2}W_2 \end{aligned} \tag{4.30}$$

where we omit the time level n in numerical fluxes, and W_1, W_2 are defined as

$$W_1 = \begin{pmatrix} \bar{\rho}_1|I^{n+1}| \\ \bar{M}_1^x|I^{n+1}| \\ \bar{M}_1^y|I^{n+1}| \\ \bar{E}_1^*|I^{n+1}| \end{pmatrix} := \bar{\boldsymbol{U}}^n|I^n| - 2\tau \sum_{m=1}^{M} |l^m| \sum_{\alpha=1}^{K} \omega_\alpha \widehat{\boldsymbol{F}} \left(\boldsymbol{U}^{\text{in}}(x_\alpha^m, y_\alpha^m), \boldsymbol{U}^{\text{ex}}(x_\alpha^m, y_\alpha^m), \boldsymbol{n}^m \right),$$

$$W_2 = \begin{pmatrix} \bar{\rho}_2|I^{n+1}| \\ \bar{M}_2^x|I^{n+1}| \\ \bar{M}_2^y|I^{n+1}| \\ \bar{E}_2^*|I^{n+1}| \end{pmatrix} := \bar{\boldsymbol{U}}^n|I^n| + 2\tau \sum_{m=1}^{M} |l^m| \sum_{\alpha=1}^{K} \omega_\alpha \widehat{\boldsymbol{G}} \left(\boldsymbol{U}^m(x_\alpha^m, y_\alpha^m), \boldsymbol{n}^m \right).$$

As before, we will prove that if we have $\boldsymbol{U}^{\text{in}}(x_{\alpha,\beta}, y_{\alpha,\beta}), \boldsymbol{U}^{\text{ex}}(x_{\alpha,\beta}, y_{\alpha,\beta}), \boldsymbol{U}^m(x_{\alpha,\beta}, y_{\alpha,\beta}) \in G,\ \forall 1 \le \alpha, \beta \le 3$, then $W_1, W_2 \in G$ under suitable time step conditions, which means $\bar{\boldsymbol{U}}^{n+1} \in G$.

The time step condition for the first term W_1 is similar with the situation in [6]. Here, we denote $\boldsymbol{U}_\alpha^{m,\text{in}} := \boldsymbol{U}^{\text{in}}(x_\alpha^m, y_\alpha^m)$, $\boldsymbol{U}_\alpha^{m,\text{ex}} := \boldsymbol{U}^{\text{ex}}(x_\alpha^m, y_\alpha^m)$ for $m = 1, \cdots, 4$ and $\alpha = 1, \cdots, K$,

and the first part W_1 can be rewritten with (4.29) as

$$
\begin{aligned}
W_1 = \quad & \frac{1}{2}\left[\sum_{\alpha=1}^{K}\sum_{\beta=2}^{K-1}\tilde{\omega}_{\alpha,\beta}\boldsymbol{U}^{\alpha,\beta}|J|^{\alpha,\beta}+\sum_{\alpha=2}^{K-1}\sum_{\beta=1}^{K}\tilde{\omega}_{\alpha,\beta}\boldsymbol{U}^{\alpha,\beta}|J|^{\alpha,\beta}\right] \\
& +\frac{1}{2}\omega_1\sum_{\alpha=1}^{K}\omega_\alpha\left(\boldsymbol{U}^{\alpha,1}|J|^{\alpha,1}+\boldsymbol{U}^{1,\alpha}|J|^{1,\alpha}+\boldsymbol{U}^{\alpha,K}|J|^{\alpha,K}+\boldsymbol{U}^{K,\alpha}|J|^{K,\alpha}\right) \\
& -2\tau\sum_{m=1}^{M}|l^m|\sum_{\alpha=1}^{K}\omega_\alpha\widehat{\boldsymbol{F}}\left(\boldsymbol{U}^{\text{in}}(x_\alpha^m,y_\alpha^m),\boldsymbol{U}^{\text{ex}}(x_\alpha^m,y_\alpha^m),\boldsymbol{n}^m\right) \\
= \quad & \frac{1}{2}\left[\sum_{\alpha=1}^{K}\sum_{\beta=2}^{K-1}\tilde{\omega}_{\alpha,\beta}\boldsymbol{U}^{\alpha,\beta}|J|^{\alpha,\beta}+\sum_{\alpha=2}^{K-1}\sum_{\beta=1}^{K}\tilde{\omega}_{\alpha,\beta}\boldsymbol{U}^{\alpha,\beta}|J|^{\alpha,\beta}\right] \\
& +\frac{1}{2}\omega_1\sum_{\alpha=1}^{K}\omega_\alpha\left(\boldsymbol{U}^{\alpha,1}|J|^{\alpha,1}+\boldsymbol{U}^{1,\alpha}|J|^{1,\alpha}+\boldsymbol{U}^{\alpha,K}|J|^{\alpha,K}+\boldsymbol{U}^{K,\alpha}|J|^{K,\alpha}\right) \\
& -2\tau|l^2|\sum_{\alpha=1}^{K}\omega_\alpha\widehat{\boldsymbol{F}}\left(\boldsymbol{U}_\alpha^{2,\text{in}},\boldsymbol{U}_\alpha^{2,\text{ex}},\boldsymbol{n}^2\right)+\boxed{2\tau|l^2|\textstyle\sum_{\alpha=1}^{K}\omega_\alpha\widehat{\boldsymbol{F}}\left(\boldsymbol{U}_\alpha^{1,\text{in}},\boldsymbol{U}_\alpha^{2,\text{in}},\boldsymbol{n}^2\right)} \\
& -2\tau|l^3|\sum_{\alpha=1}^{K}\omega_\alpha\widehat{\boldsymbol{F}}\left(\boldsymbol{U}_\alpha^{3,\text{in}},\boldsymbol{U}_\alpha^{3,\text{ex}},\boldsymbol{n}^3\right)+\boxed{2\tau|l^3|\textstyle\sum_{\alpha=1}^{K}\omega_\alpha\widehat{\boldsymbol{F}}\left(\boldsymbol{U}_\alpha^{1,\text{in}},\boldsymbol{U}_\alpha^{3,\text{in}},\boldsymbol{n}^3\right)} \\
& -2\tau|l^4|\sum_{\alpha=1}^{K}\omega_\alpha\widehat{\boldsymbol{F}}\left(\boldsymbol{U}_\alpha^{4,\text{in}},\boldsymbol{U}_\alpha^{4,\text{ex}},\boldsymbol{n}^4\right)+\boxed{2\tau|l^4|\textstyle\sum_{\alpha=1}^{K}\omega_\alpha\widehat{\boldsymbol{F}}\left(\boldsymbol{U}_\alpha^{1,\text{in}},\boldsymbol{U}_\alpha^{4,\text{in}},\boldsymbol{n}^4\right)} \\
& -2\tau|l^1|\sum_{\alpha=1}^{K}\omega_\alpha\widehat{\boldsymbol{F}}\left(\boldsymbol{U}_\alpha^{1,\text{in}},\boldsymbol{U}_\alpha^{1,\text{ex}},\boldsymbol{n}^1\right) \\
& -2\tau\sum_{\alpha=1}^{K}\omega_\alpha\boxed{\left[|l^2|\widehat{\boldsymbol{F}}\left(\boldsymbol{U}_\alpha^{1,\text{in}},\boldsymbol{U}_\alpha^{2,\text{in}},\boldsymbol{n}^2\right)+|l^3|\widehat{\boldsymbol{F}}\left(\boldsymbol{U}_\alpha^{1,\text{in}},\boldsymbol{U}_\alpha^{3,\text{in}},\boldsymbol{n}^3\right)+|l^4|\widehat{\boldsymbol{F}}\left(\boldsymbol{U}_\alpha^{1,\text{in}},\boldsymbol{U}_\alpha^{4,\text{in}},\boldsymbol{n}^4\right)\right]} \\
= \quad & \frac{1}{2}\left[\sum_{\alpha=1}^{K}\sum_{\beta=2}^{K-1}\tilde{\omega}_{\alpha,\beta}\boldsymbol{U}^{\alpha,\beta}|J|^{\alpha,\beta}+\sum_{\alpha=2}^{K-1}\sum_{\beta=1}^{K}\tilde{\omega}_{\alpha,\beta}\boldsymbol{U}^{\alpha,\beta}|J|^{\alpha,\beta}\right] \\
& +\frac{\omega_1}{2}\sum_{\alpha=1}^{K}\omega_\alpha\left(\hat{\mathcal{F}}_\alpha^1+\hat{\mathcal{F}}_\alpha^2+\hat{\mathcal{F}}_\alpha^3+\hat{\mathcal{F}}_\alpha^4\right).
\end{aligned}
\tag{4.31}
$$

where

$$\begin{aligned}
\hat{\mathcal{F}}_\alpha^1 :=\ & |J|^{\alpha,1}\boldsymbol{U}_\alpha^{1,\text{in}} - \frac{4\tau}{\omega_1}|l^1|\widehat{\boldsymbol{F}}(\boldsymbol{U}_\alpha^{1,\text{in}},\boldsymbol{U}_\alpha^{1,\text{ex}},\boldsymbol{n}^1) \\
& - \frac{4\tau}{\omega_1}\left[|l^2|\widehat{\boldsymbol{F}}(\boldsymbol{U}_\alpha^{1,\text{in}},\boldsymbol{U}_\alpha^{2,\text{in}},\boldsymbol{n}^2) + |l^3|\widehat{\boldsymbol{F}}(\boldsymbol{U}_\alpha^{1,\text{in}},\boldsymbol{U}_\alpha^{3,\text{in}},\boldsymbol{n}^3) + |l^4|\widehat{\boldsymbol{F}}(\boldsymbol{U}_\alpha^{1,\text{in}},\boldsymbol{U}_\alpha^{4,\text{in}},\boldsymbol{n}^4)\right], \\
\hat{\mathcal{F}}_\alpha^2 :=\ & |J|^{K,\alpha}\boldsymbol{U}_\alpha^{2,\text{in}} - \frac{4\tau|l^2|}{\omega_1}\left[\widehat{\boldsymbol{F}}(\boldsymbol{U}_\alpha^{2,\text{in}},\boldsymbol{U}_\alpha^{2,\text{ex}},\boldsymbol{n}^2) - \widehat{\boldsymbol{F}}(\boldsymbol{U}_\alpha^{1,\text{in}},\boldsymbol{U}_\alpha^{2,\text{in}},\boldsymbol{n}^2)\right], \\
\hat{\mathcal{F}}_\alpha^3 :=\ & |J|^{\alpha,K}\boldsymbol{U}_\alpha^{3,\text{in}} - \frac{4\tau|l^3|}{\omega_1}\left[\widehat{\boldsymbol{F}}(\boldsymbol{U}_\alpha^{3,\text{in}},\boldsymbol{U}_\alpha^{3,\text{ex}},\boldsymbol{n}^3) - \widehat{\boldsymbol{F}}(\boldsymbol{U}_\alpha^{1,\text{in}},\boldsymbol{U}_\alpha^{3,\text{in}},\boldsymbol{n}^3)\right], \\
\hat{\mathcal{F}}_\alpha^4 :=\ & |J|^{1,\alpha}\boldsymbol{U}_\alpha^{4,\text{in}} - \frac{4\tau|l^4|}{\omega_1}\left[\widehat{\boldsymbol{F}}(\boldsymbol{U}_\alpha^{4,\text{in}},\boldsymbol{U}_\alpha^{4,\text{ex}},\boldsymbol{n}^4) - \widehat{\boldsymbol{F}}(\boldsymbol{U}_\alpha^{1,\text{in}},\boldsymbol{U}_\alpha^{4,\text{in}},\boldsymbol{n}^4)\right].
\end{aligned}$$

Thus, we have $W_1 \in G$ under the following restriction

$$\tau \le \lambda\frac{\omega_1}{4}\min_{i,j,\alpha,\beta}\left\{\frac{|J|_{i,j}}{\sum_{m=1}^4|l_{i,j}^m|}\Big/\max\left\{a^*,\left|\frac{p^*}{\rho\sqrt{2e^*}}\right|\right\}_{i,j}^{\alpha,\beta}\right\} \tag{4.32}$$

where $|J|_{i,j} = \min\limits_{\alpha=1,K}\{|J|_{i,j}^{\alpha,1}, |J|_{i,j}^{\alpha,K}, |J|_{i,j}^{1,\alpha}, |J|_{i,j}^{K,\alpha}\}$, and $\lambda = 0.5$. Actually, $\hat{\mathcal{F}}_\alpha^2, \hat{\mathcal{F}}_\alpha^3, \hat{\mathcal{F}}_\alpha^4 \in G$ are the same as the situation for the one-dimensional first order scheme, and one can refer to [7] for the details. For $\hat{\mathcal{F}}_\alpha^1$, we can use the same trick in (4.24) to verify that $\hat{\mathcal{F}}_\alpha^1 \in G$ by adding

$$\sum_{m=1}^4\widehat{\boldsymbol{F}}(\boldsymbol{U}_\alpha^{1,\text{in}},\boldsymbol{U}_\alpha^{1,\text{in}},\boldsymbol{n}^m)|l^m| = \sum_{m=1}^4\boldsymbol{F}(\boldsymbol{U}_\alpha^{1,\text{in}},\boldsymbol{n}^m)|l^m| = 0.$$

As for the diffusion term, the first three terms in the numerical flux $\widehat{\boldsymbol{G}}(\boldsymbol{U}_\alpha^m,\boldsymbol{n})$ are zeros which means the cell averages of density in the second part are positive, $\bar{\rho}_2 = \bar{\rho}^n > 0$ and

$$\begin{aligned}
\bar{e}_2^* =\ & \bar{E}_2^* - \frac{1}{2}\frac{(\bar{M}_2^x)^2 + (\bar{M}_2^y)^2}{\bar{\rho}_2} \\
=\ & \bar{E}^{*,n} + 2\tau\sum_{m=1}^M\frac{|l^m|}{|I^n|}\sum_{\alpha=1}^K\omega_\alpha\hat{g}\left(\boldsymbol{U}_\alpha^m,\boldsymbol{n}^m\right) - \frac{1}{2}\frac{(\bar{M}^{x,n})^2 + (\bar{M}^{y,n})^2}{\bar{\rho}^n} \\
=\ & \bar{e}^{*,n} + 2\tau\sum_{m=1}^M\frac{|l^m|}{|I^n|}\sum_{\alpha=1}^K\omega_\alpha\hat{g}\left(\boldsymbol{U}_\alpha^m,\boldsymbol{n}^m\right)
\end{aligned}$$

where $\hat{g}(\boldsymbol{U}_\alpha^m,\boldsymbol{n}^m) := \kappa n_x^m\partial_x T^4(\boldsymbol{U}_\alpha^m) + \kappa n_y^m\partial_y T^4(\boldsymbol{U}_\alpha^m)$.

Just like before, we separate the cell average and give a suitable time step condition for

the positivity of the total internal energy $\bar{e}_2^*$,

$$\begin{aligned}
\bar{e}_2^*|I^n| = & \frac{1}{2}\left[\sum_{\alpha=1}^{K}\sum_{\beta=2}^{K-1}\tilde{\omega}_{\alpha,\beta}e^{*,\alpha,\beta}|J|^{\alpha,\beta}+\sum_{\alpha=2}^{K-1}\sum_{\beta=1}^{K}\tilde{\omega}_{\alpha,\beta}e^{*,\alpha,\beta}|J|^{\alpha,\beta}\right] \\
& +\frac{1}{2}\omega_1\sum_{\alpha=1}^{K}\omega_\alpha\left(e^{*,\alpha,1}|J|^{\alpha,1}+e^{*,1,\alpha}|J|^{1,\alpha}+e^{*,\alpha,K}|J|^{\alpha,K}+e^{*,K,\alpha}|J|^{K,\alpha}\right) \\
& +2\tau\sum_{m=1}^{M}|l^m|\sum_{\alpha=1}^{K}\omega_\alpha\hat{g}\left(\boldsymbol{U}_\alpha^m,\boldsymbol{n}^m\right) \\
= & \frac{1}{2}\left[\sum_{\alpha=1}^{K}\sum_{\beta=2}^{K-1}\tilde{\omega}_{\alpha,\beta}e^{*,\alpha,\beta}|J|^{\alpha,\beta}+\sum_{\alpha=2}^{K-1}\sum_{\beta=1}^{K}\tilde{\omega}_{\alpha,\beta}e^{*,\alpha,\beta}|J|^{\alpha,\beta}\right] \\
& +\frac{\omega_1}{2}\sum_{\alpha=1}^{K}\omega_\alpha\left(\hat{\mathcal{G}}_\alpha^1+\hat{\mathcal{G}}_\alpha^2+\hat{\mathcal{G}}_\alpha^3+\hat{\mathcal{G}}_\alpha^4\right)
\end{aligned}$$

where $\hat{\mathcal{G}}_\alpha^1 := |J|^{\alpha,1}e^{*,\alpha,1}+\frac{4\tau}{\omega_1}|l^1|\hat{g}(\boldsymbol{U}_\alpha^1,\boldsymbol{n}^1)$, and $\hat{\mathcal{G}}_\alpha^2,\hat{\mathcal{G}}_\alpha^3,\hat{\mathcal{G}}_\alpha^4$ are defined in the similar way. As we have discussed in (4.27), we can deduce that $\bar{e}_2^*$ is positive and $W_2\in G$, if

$$\tau\le\lambda\frac{\omega_1}{4\kappa}\min_{i,j,\alpha,\beta}\left\{\left|\frac{J}{l}\right|_{i,j}\cdot\frac{e_{i,j}^{*,\alpha,\beta}}{\varepsilon+\sqrt{2}\max\limits_{m}\left\{|\partial_x T^4(\boldsymbol{U}_{i,j,\alpha,\beta}^m)|,|\partial_y T^4(\boldsymbol{U}_{i,j,\alpha,\beta}^m)|\right\}}\right\}, \tag{4.33}$$

where $\left|\frac{J}{l}\right|_{i,j}=\min\limits_{\alpha=1,K}\{\frac{|J|_{i,j}^{\alpha,1}}{|l_{i,j}^1|},\frac{|J|_{i,j}^{K,\alpha}}{|l_{i,j}^2|},\frac{|J|_{i,j}^{\alpha,K}}{|l_{i,j}^3|},\frac{|J|_{i,j}^{1,\alpha}}{|l_{i,j}^4|}\}$, $\varepsilon=10^{-13}$ is a small positive constant and $\lambda=0.5$.

Since the admissible set G is convex, then we have the following theorem.

Theorem 4.2. *Consider the high-order explicit Lagrangian finite volume method (3.15) solving (2.1) with the HLLC numerical flux. If the values of the high-order reconstruction polynomials $\boldsymbol{U}_{i,j}^n(x,y)$, $\boldsymbol{U}_{i,j}^{n,m}(x,y)$ satisfy $\boldsymbol{U}_{i,j}^n(x_{\alpha,\beta},y_{\alpha,\beta})\in G$ and $\boldsymbol{U}_{i,j}^{n,m}(x_{\alpha,\beta},y_{\alpha,\beta})\in G$ for all of the quadrature points $(x_{\alpha,\beta},y_{\alpha,\beta})$ at the time level $t=t^n$, then the new cell averages $\bar{\boldsymbol{U}}_{i,j}^{n+1}\in G$ preserving positivity under the time step constraints (4.32) and (4.33).*

Based on the above theorem, we can use the positivity-preserving limiter proposed by Zhang and Shu [26, 27] to ensure $\boldsymbol{U}_{i,j}^n(x_{\alpha,\beta},y_{\alpha,\beta})\in G$ and $\boldsymbol{U}_{i,j}^{n,m}(x_{\alpha,\beta},y_{\alpha,\beta})\in G$. Suppose the cell-averages $\bar{\boldsymbol{U}}_{i,j}^n=(\bar{\rho}_{i,j},\bar{M}_{i,j}^x,\bar{M}_{i,j}^y,\bar{E}_{i,j}^*)^T$ are in the admissible set $\bar{\boldsymbol{U}}_{i,j}^n\in G$, we will modify the multi-resolution WENO reconstruction polynomials

$$\boldsymbol{U}_{i,j}^n(x,y)=(\rho(x,y),M^x(x,y),M^y(x,y),E^*(x,y))_{i,j}^{n,T}$$

into $\tilde{\boldsymbol{U}}_{i,j}^n(x,y)$ such that $\tilde{\boldsymbol{U}}_{i,j}^n(x_{\alpha,\beta},y_{\alpha,\beta}) \in G$, $\forall (x_{\alpha,\beta},y_{\alpha,\beta}) \in I_{i,j}$. The modification has the following two steps

1. *Preserve positivity for density.* For each cell $I_{i,j}$, define

$$\hat{\rho}_{i,j}^n(x,y) = \theta_{i,j}^1 \rho_{i,j}^n(x,y) + (1-\theta_{i,j}^1)\bar{\rho}_{i,j}^n, \quad \theta_{i,j}^1 = \min_{(x,y)\in S_{i,j}} \left\{1, \left|\frac{\bar{\rho}_{i,j}^n - \varepsilon}{\bar{\rho}_{i,j}^n - \rho_{i,j}^n(x,y)}\right|\right\} \tag{4.34}$$

   where $\bar{\rho}_{i,j}^n \geq \varepsilon$, $\forall i,j$ and we will take $\varepsilon = 10^{-13}$. $S_{i,j}$ is the set of the quadrature points $(x_{\alpha,\beta},y_{\alpha,\beta})$ on $I_{i,j}$.

2. *Preserve positivity for internal energy.* After the first step, define

$$\hat{\boldsymbol{U}}_{i,j}^n(x,y) = (\hat{\rho}(x,y), M^x(x,y), M^y(x,y), E^*(x,y))_{i,j}^{n,T},$$

   then the final modified polynomial is obtained as

$$\begin{aligned} \tilde{\boldsymbol{U}}_{i,j}^n(x,y) = &\ \theta_{i,j}^2 \hat{\boldsymbol{U}}_{i,j}^n(x,y) + (1-\theta_{i,j}^2)\bar{\boldsymbol{U}}_{i,j}^n, \\ \theta_{i,j}^2 = &\ \min_{(x,y)\in S_{i,j}} \left\{1, \left|\frac{\bar{e}_{i,j}^{*,n}}{\bar{e}_{i,j}^{*,n} - e^{*,n}(\hat{\boldsymbol{U}}_{i,j}^n(x,y))}\right|\right\}. \end{aligned} \tag{4.35}$$

Then, we could use the same recipe to preserve positivity for $\boldsymbol{U}_{i,j}^{n,m}(x,y)$, such that $\tilde{\boldsymbol{U}}_{i,j}^{n,m}(x_{\alpha,\beta},y_{\alpha,\beta}) \in G$. It is obvious that this positivity-preserving limiter can keep conservation, and it can preserve positivity for density and internal energy with admissible cell averages $\bar{\boldsymbol{U}}_{i,j}^n \in G$. In [25], the authors proved that this limiter will not destroy the original high order accuracy, and we will verify these good properties via some numerical experiments in Section 6.

5 The explicit-implicit-null Lagrangian finite volume scheme

In Section 3, we have introduced the explicit Lagrangian scheme but the time step is limited by the diffusion term $\tau_{diff} = \mathcal{O}(\frac{h^2}{\kappa})$ in (3.21), which is rather severe, especially when κ is not very small. The authors of [7] employed the implicit-explicit (IMEX) method to relieve the constraints imposed by the radiation diffusion. Specifically, they treated the advection

term explicitly and the diffusion term implicitly, to address this issue. However, the Newton iteration method for the implicit nonlinear diffusion term results in a high computational cost and significant memory consumption, especially for higher dimensional problems.

The explicit-implicit-null (EIN) [23, 21] time-marching method is designed to cope with this shortcoming, where one adds a sufficiently large linear artificial diffusion term on both sides of the scheme, and then solves the nonlinear diffusion term and the advection term explicitly, and solve the artificial linear term on the right-hand side implicitly which is easy to handle with the IMEX method. In this section, we will introduce the EIN Lagrangian finite volume scheme for the two-dimensional RHE (2.1). Since the first three variables in the diffusion term are zero, so we use $\boldsymbol{H}_1(\boldsymbol{U}) = (0, 0, 0, \partial_x E^*)^T$ and $\boldsymbol{H}_2(\boldsymbol{U}) = (0, 0, 0, \partial_y E^*)^T$ to denote the artificial diffusion terms.

By adding $a_0\partial_x \boldsymbol{H}_1 + b_0\partial_y \boldsymbol{H}_2$ to both sides of (2.3), we have

$$\begin{aligned} & \boldsymbol{U}_t + \partial_x \boldsymbol{F}_1 + \partial_y \boldsymbol{F}_2 = \partial_x \boldsymbol{G}_1 + \partial_y \boldsymbol{G}_2 \\ \Rightarrow \quad & \boldsymbol{U}_t + \partial_x \boldsymbol{F}_1 + \partial_y \boldsymbol{F}_2 - \partial_x \boldsymbol{G}_1 - \partial_y \boldsymbol{G}_2 + \boxed{a_0\partial_x \boldsymbol{H}_1 + b_0\partial_y \boldsymbol{H}_2} = \boxed{a_0\partial_x \boldsymbol{H}_1 + b_0\partial_y \boldsymbol{H}_2} \end{aligned}$$

and it can be expressed in integral form just like (3.9) as

$$\frac{d}{dt}\int_{\Omega(t)} \boldsymbol{U} d\Omega + \int_{\Gamma(t)} \boldsymbol{F} d\Gamma - \int_{\Gamma(t)} \boldsymbol{G} d\Gamma + \int_{\Gamma(t)} \boldsymbol{H} d\Gamma = \int_{\Gamma(t)} \boldsymbol{H} d\Gamma \tag{5.36}$$

where $\boldsymbol{H}(\boldsymbol{U}) = (0, 0, 0, a_0 n_x \partial_x E^* + b_0 n_y \partial_y E^*)^T$. In [21], by the aid of the Fourier method, the authors analyzed stability for the EIN schemes, so we follow their idea and take the parameter a_0, b_0 as

$$a_0 = b_0 = a_{EIN} \max \left| \frac{\partial \kappa T^4}{\partial E^*} \right|, \quad a_{EIN} = 1.$$

Then, just like the explicit Lagrangian scheme (3.15) with the Euler forward time discretization, we treat the nonlinear terms $\boldsymbol{F}$, $\boldsymbol{G}$ and the left-hand side linear term $\boldsymbol{H}$ explicitly,

and the right-hand side linear term $\boldsymbol{H}$ implicitly,

$$
\begin{aligned}
&\bar{\boldsymbol{U}}_{i,j}^{n+1}|I_{i,j}^{n+1}| - \bar{\boldsymbol{U}}_{i,j}^{n}|I_{i,j}| \\
=&\tau \int_{\partial I_{i,j}} \left(-\widehat{\boldsymbol{F}}^n + \widehat{\boldsymbol{G}}^n - \widehat{\boldsymbol{H}}^n\right) dl + \tau \int_{\partial I_{i,j}} \widehat{\boldsymbol{H}}^{n+1} dl \\
=&-\tau \sum_{m=1}^{M} |l^m| \sum_{\alpha=1}^{K} \omega_\alpha \widehat{\boldsymbol{F}} \left(\boldsymbol{U}^{n,\text{in}}(x_\alpha^m, y_\alpha^m), \boldsymbol{U}^{n,\text{ex}}(x_\alpha^m, y_\alpha^m), \boldsymbol{n}^m\right) \\
&+\tau \sum_{m=1}^{M} |l^m| \sum_{\alpha=1}^{K} \omega_\alpha \widehat{\boldsymbol{G}} \left(\boldsymbol{U}^{n,m}(x_\alpha^m, y_\alpha^m), \boldsymbol{n}^m\right) \\
&-\tau \sum_{m=1}^{M} |l^m| \sum_{\alpha=1}^{K} \omega_\alpha \widehat{\boldsymbol{H}} \left(\boldsymbol{U}^{n,\text{in}}(x_\alpha^m, y_\alpha^m), \boldsymbol{U}^{n,\text{ex}}(x_\alpha^m, y_\alpha^m), \boldsymbol{n}^m\right) \\
&+\tau \sum_{m=1}^{M} |l^m| \sum_{\alpha=1}^{K} \omega_\alpha \widehat{\boldsymbol{H}} \left(\boldsymbol{U}^{n+1,\text{in}}(x_\alpha^m, y_\alpha^m), \boldsymbol{U}^{n+1,\text{ex}}(x_\alpha^m, y_\alpha^m), \boldsymbol{n}^m\right)
\end{aligned}
\tag{5.37}
$$

Here, we use the central numerical flux for the artificial diffusion terms

$$
\begin{aligned}
&\widehat{\boldsymbol{H}}(\boldsymbol{U}^{n,\text{in}}(x_\alpha^m, y_\alpha^m), \boldsymbol{U}^{n,\text{ex}}(x_\alpha^m, y_\alpha^m), \boldsymbol{n}^m) \\
=&\frac{a_0}{2} n_x^m \left[\partial_x \boldsymbol{H}(\boldsymbol{U}^{n,\text{in}}(x_\alpha^m, y_\alpha^m)) + \partial_x \boldsymbol{H}(\boldsymbol{U}^{n,\text{ex}}(x_\alpha^m, y_\alpha^m))\right] \\
&+\frac{b_0}{2} n_y^m \left[\partial_y \boldsymbol{H}(\boldsymbol{U}^{n,\text{in}}(x_\alpha^m, y_\alpha^m)) + \partial_y \boldsymbol{H}(\boldsymbol{U}^{n,\text{ex}}(x_\alpha^m, y_\alpha^m))\right],
\end{aligned}
\tag{5.38}
$$

similarly for $\widehat{\boldsymbol{H}}(\boldsymbol{U}^{n+1,\text{in}}(x_\alpha^m, y_\alpha^m), \boldsymbol{U}^{n+1,\text{ex}}(x_\alpha^m, y_\alpha^m), \boldsymbol{n}^m)$. Notice that, in order not to introduce extra error in space, we should use the same spatial discretization for $\widehat{\boldsymbol{H}}^n$ and $\widehat{\boldsymbol{H}}^{n+1}$. The details of the reconstruction for the polynomials in the artificial diffusion terms $\widehat{\boldsymbol{H}}^n$ and $\widehat{\boldsymbol{H}}^{n+1}$ are put in the Appendix A.3. This EIN scheme avoids solving the radiation diffusion explicitly with a small time scale. Compared with the other implicit methods, such as the IMEX method, it also avoids from solving the nonlinear diffusion term implicitly, which would need a computationally expensive Newton iteration in the IMEX method.

5.1 The EIN Lagrangian finite volume scheme

Denote the explicit nonlinear part as

$$
\mathcal{N}_{i,j}(\bar{\boldsymbol{U}}^n) := \int_{\partial I_{i,j}} (-\widehat{\boldsymbol{F}}^n + \widehat{\boldsymbol{G}}^n - \widehat{\boldsymbol{H}}^n) dl
$$

and the implicit linear part as

$$\mathcal{L}_{i,j}(\bar{\boldsymbol{U}}^{n+1}) := \int_{\partial I_{i,j}} \widehat{\boldsymbol{H}}^{n+1} dl,$$

the first-order EIN scheme (5.37) can be written as

$$\begin{aligned}
&x^{n+1}_{i+\frac{1}{2},j+\frac{1}{2}} = x^{n}_{i+\frac{1}{2},j+\frac{1}{2}} + \tau u^{n}_{i+\frac{1}{2},j+\frac{1}{2}},\\
&y^{n+1}_{i+\frac{1}{2},j+\frac{1}{2}} = y^{n}_{i+\frac{1}{2},j+\frac{1}{2}} + \tau v^{n}_{i+\frac{1}{2},j+\frac{1}{2}},\\
&\bar{\boldsymbol{U}}^{n+1}_{i,j}|I^{n+1}_{i,j}| - \bar{\boldsymbol{U}}^{n}_{i,j}|I^{n}_{i,j}| = \tau\mathcal{N}_{i,j}(\bar{\boldsymbol{U}}^{n}) + \tau\mathcal{L}_{i,j}(\bar{\boldsymbol{U}}^{n+1}).
\end{aligned} \tag{5.39}$$

Refer to [23], the third-order EIN Lagrangian scheme follows as

- Step 1.

$$\begin{aligned}
&x^{(1)}_{i+\frac{1}{2},j+\frac{1}{2}} = x^{n}_{i+\frac{1}{2},j+\frac{1}{2}}, \quad y^{(1)}_{i+\frac{1}{2},j+\frac{1}{2}} = y^{n}_{i+\frac{1}{2},j+\frac{1}{2}},\\
&\bar{\boldsymbol{U}}^{(1)}_{i,j}|I^{(1)}_{i,j}| = \bar{\boldsymbol{U}}^{n}_{i,j}|I^{n}_{i,j}| + \alpha\tau\mathcal{L}_{i,j}(\bar{\boldsymbol{U}}^{(1)}).
\end{aligned}$$

- Step 2.

$$\begin{aligned}
&x^{(2)}_{i+\frac{1}{2},j+\frac{1}{2}} = x^{n}_{i+\frac{1}{2},j+\frac{1}{2}}, \quad y^{(2)}_{i+\frac{1}{2},j+\frac{1}{2}} = y^{n}_{i+\frac{1}{2},j+\frac{1}{2}},\\
&\bar{\boldsymbol{U}}^{(2)}_{i,j}|I^{(2)}_{i,j}| = \bar{\boldsymbol{U}}^{n}_{i,j}|I^{n}_{i,j}| + \alpha\tau\left[-\mathcal{L}_{i,j}(\bar{\boldsymbol{U}}^{(1)}) + \mathcal{L}_{i,j}(\bar{\boldsymbol{U}}^{(2)})\right].
\end{aligned}$$

- Step 3.

$$\begin{aligned}
&x^{(3)}_{i+\frac{1}{2},j+\frac{1}{2}} = x^{n}_{i+\frac{1}{2},j+\frac{1}{2}} + \tau u^{(2)}_{i+\frac{1}{2},j+\frac{1}{2}},\\
&y^{(3)}_{i+\frac{1}{2},j+\frac{1}{2}} = y^{n}_{i+\frac{1}{2},j+\frac{1}{2}} + \tau v^{(2)}_{i+\frac{1}{2},j+\frac{1}{2}},\\
&\bar{\boldsymbol{U}}^{(3)}_{i,j}|I^{(3)}_{i,j}| = \bar{\boldsymbol{U}}^{n}_{i,j}|I^{n}_{i,j}| + \tau\left[\mathcal{N}_{i,j}(\bar{\boldsymbol{U}}^{(2)}) + (1-\alpha)\mathcal{L}_{i,j}(\bar{\boldsymbol{U}}^{(2)}) + \alpha\mathcal{L}_{i,j}(\bar{\boldsymbol{U}}^{(3)})\right].
\end{aligned}$$

- Step 4.

$$\begin{aligned}
&x^{(4)}_{i+\frac{1}{2},j+\frac{1}{2}} = x^{n}_{i+\frac{1}{2},j+\frac{1}{2}} + \frac{\tau}{4}\left(u^{(2)}_{i+\frac{1}{2},j+\frac{1}{2}} + u^{(3)}_{i+\frac{1}{2},j+\frac{1}{2}}\right),\\
&y^{(4)}_{i+\frac{1}{2},j+\frac{1}{2}} = y^{n}_{i+\frac{1}{2},j+\frac{1}{2}} + \frac{\tau}{4}\left(v^{(2)}_{i+\frac{1}{2},j+\frac{1}{2}} + v^{(3)}_{i+\frac{1}{2},j+\frac{1}{2}}\right),\\
&\bar{\boldsymbol{U}}^{(4)}_{i,j}|I^{(4)}_{i,j}| = \bar{\boldsymbol{U}}^{n}_{i,j}|I^{n}_{i,j}| + \tau\left[\frac{1}{4}\mathcal{N}_{i,j}(\bar{\boldsymbol{U}}^{(2)}) + \frac{1}{4}\mathcal{N}_{i,j}(\bar{\boldsymbol{U}}^{(3)})\right.\\
&\quad\left.+\beta\mathcal{L}_{i,j}(\bar{\boldsymbol{U}}^{(1)}) + \xi\mathcal{L}_{i,j}(\bar{\boldsymbol{U}}^{(2)}) + \eta\mathcal{L}_{i,j}(\bar{\boldsymbol{U}}^{(3)}) + \alpha\mathcal{L}_{i,j}(\bar{\boldsymbol{U}}^{(4)})\right].
\end{aligned}$$

- Step 5.

$$\begin{aligned}
&x^{n+1}_{i+\frac{1}{2},j+\frac{1}{2}} = x^{n}_{i+\frac{1}{2},j+\frac{1}{2}} + \frac{\tau}{6}\left(u^{(2)}_{i+\frac{1}{2},j+\frac{1}{2}} + u^{(3)}_{i+\frac{1}{2},j+\frac{1}{2}} + 4u^{(4)}_{i+\frac{1}{2},j+\frac{1}{2}}\right),\\
&y^{n+1}_{i+\frac{1}{2},j+\frac{1}{2}} = y^{n}_{i+\frac{1}{2},j+\frac{1}{2}} + \frac{\tau}{6}\left(v^{(2)}_{i+\frac{1}{2},j+\frac{1}{2}} + v^{(3)}_{i+\frac{1}{2},j+\frac{1}{2}} + 4v^{(4)}_{i+\frac{1}{2},j+\frac{1}{2}}\right),\\
&\bar{\boldsymbol{U}}^{n+1}_{i,j}|I^{(n+1)}_{i,j}| = \bar{\boldsymbol{U}}^{n}_{i,j}|I^{n}_{i,j}| + \frac{\tau}{6}\left[\mathcal{N}_{i,j}(\bar{\boldsymbol{U}}^{(2)}) + \mathcal{N}_{i,j}(\bar{\boldsymbol{U}}^{(3)}) + 4\mathcal{N}_{i,j}(\bar{\boldsymbol{U}}^{(4)})\right.\\
&\quad\left.+\mathcal{L}_{i,j}(\bar{\boldsymbol{U}}^{(2)}) + \mathcal{L}_{i,j}(\bar{\boldsymbol{U}}^{(3)}) + 4\mathcal{L}_{i,j}(\bar{\boldsymbol{U}}^{(4)})\right].
\end{aligned}$$

where $\alpha = 0.241694261$, $\beta = \frac{\alpha}{4}$, $\xi = \frac{1}{4} - 2\beta$, $\eta = \frac{1}{2} - \alpha - \beta - \xi$.

So far, we have presented two high-order Lagrangian finite volume schemes. Notably, the EIN Lagrangian scheme is highly accurate and efficient, but it cannot adequately handle sharp discontinuities yet since we do not apply the WENO idea to the implicit part of the scheme. In the next section, we will verify the good properties of the two types of Lagrangian schemes in different situations.

6 Numerical tests

In this section, we perform a series of numerical tests on our explicit Lagrangian finite volume scheme and the EIN Lagrangian finite volume scheme, to verify their second-order accuracy and some other good properties. Notice that, even though we are using third order reconstructions and third order time discretization, because we use cells with straight-line edges, our Lagrangian scheme is restricted to second order accuracy so far [5] . Curved cells would be needed to obtain third or higher order of accuracy, but we will not discuss it in this paper. For brevity, we will denote these two schemes as the "explicit scheme" and the "EIN scheme", respectively.

6.1 Accuracy test

Consider the radiation hydrodynamics equations in the equilibrium-diffusion limit (2.3) with the source term $\boldsymbol{s} = (s_1(x,y,t), s_2(x,y,t), s_3(x,y,t), s_4(x,y,t))^T$ on the computational domain $\Omega = [0, 2\pi] \times [0, 2\pi]$,

$$\partial_t \boldsymbol{U} + \partial_x \boldsymbol{F}_1(\boldsymbol{U}) + \partial_y \boldsymbol{F}_2(\boldsymbol{U}) = \partial_x \boldsymbol{G}_1(\boldsymbol{U}) + \partial_y \boldsymbol{G}_2(\boldsymbol{U}) + \boldsymbol{s}$$

with the exact solution

$$\begin{cases} \rho(x,t) &= 1 + 0.5\sin(x+y-2t), \\ u(x,t) &= 0.5 + \cos(x+y-2t), \\ v(x,t) &= 0.5 + \cos(x+y-2t), \\ T(x,t) &= b_1(1 + b_2\sin(x+y-2t)), \end{cases}$$

where $b_1,\ b_2$ are constants.

Be aware that, for the γ-law gas

$$p^* = (\gamma-1)c_v\rho T + \frac{1}{3}\mathcal{P}T^4, \quad E^* = c_v\rho T + \frac{1}{2}\rho u^2 + \frac{1}{2}\rho v^2 + \mathcal{P}T^4,$$

so we have

$$\begin{aligned}
s_1 &= 2\sin(2t-x-y) - 0.5\cos(2t-x-y) + \cos(4t-2(x+y)) \\
s_2 &= \cos(2t-x-y)\left[-\tfrac{1}{4} - 0.5b_1c_v - b_1b_2c_v + \tfrac{1}{2}b_1c_v\gamma + b_1b_2c_v\gamma + \tfrac{4}{3}b_1^4b_2\mathcal{P}\right. \\
&\quad + \cos^2(2t-x-y) + (4 + b_1b_2c_v(1-\gamma) - 4b_1^4b_2^2\mathcal{P})\sin(2t-x-y) \\
&\quad \left. + (-2 + 4b_1^4b_2^3\mathcal{P})\sin^2(2t-x-y) - \tfrac{4}{3}b_1^4b_2^4\mathcal{P}\sin^3(2t-x-y)\right] \\
s_3 &= \cos(2t-x-y)\left[-\tfrac{1}{4} - \tfrac{b_1c_v}{2} - b_1b_2c_v + \tfrac{1}{2}b_1c_v\gamma + b_1b_2c_v\gamma + \tfrac{4}{3}b_1^4b_2\mathcal{P}\right. \\
&\quad + \cos^2(2t-x-y) + (4 + b_1b_2c_v(1-\gamma) - 4b_1^4b_2^2\mathcal{P})\sin(2t-x-y) \\
&\quad \left. + (-2 + 4b_1^4b_2^3\mathcal{P})\sin^2(2t-x-y) - \tfrac{4}{3}b_1^4b_2^4\mathcal{P}\sin^3(2t-x-y)\right]
\end{aligned}$$

and

$$\begin{aligned}
s_4 &= \tfrac{1}{2}\cos^3(2t-x-y) + \cos^4(2t-x-y) \\
&\quad -24\cos^2(2t-x-y)\left[\tfrac{1}{96} + b_1(-\tfrac{1}{24} - \tfrac{b_2}{12})c_v\gamma + b_1^4b_2(b_2\kappa - \tfrac{4\mathcal{P}}{9})\right. \\
&\quad + \sin(2t-x-y)\left(-\tfrac{1}{4} + \tfrac{1}{12}b_1b_2c_v\gamma + b_1^4b_2^2\left(-2b_2\kappa + \tfrac{4\mathcal{P}}{3}\right)\right) \\
&\quad \left. + \sin^2(2t-x-y)\left(\tfrac{1}{8} + b_1^4b_2^3(b_2\kappa - \tfrac{4\mathcal{P}}{3})\right) + \tfrac{4}{9}b_1^4b_2^4\mathcal{P}\sin^3(2t-x-y)\right] \\
&\quad + \cos(2t-x-y)\left[-\tfrac{1}{8} + b_1c_v(-1 - 2b_2 + \tfrac{\gamma}{2} + b_2\gamma) - \tfrac{8}{3}b_1^4b_2\mathcal{P}\right. \\
&\quad + (2 + b_1b_2c_v(2-\gamma) + 8b_1^4b_2^2\mathcal{P})\sin(2t-x-y) \\
&\quad \left. + (-1 - 8b_1^4b_2^3\mathcal{P})\sin^2(2t-x-y) + \tfrac{8}{3}b_1^4b_2^4\mathcal{P}\sin^3(2t-x-y)\right] \\
&\quad + \tfrac{8}{3}\sin(2t-x-y)\left[-\tfrac{3}{16} + \tfrac{3b_1c_v\gamma}{4} + b_1^4(\mathcal{P} - 3b_2\kappa)\right. \\
&\quad + \left(\tfrac{3}{32} + b_1(-\tfrac{3}{8} - \tfrac{3b_2}{4})c_v\gamma + b_1^4b_2(9b_2\kappa - 4\mathcal{P})\right)\sin(2t-x-y) \\
&\quad + b_1b_2\left(\tfrac{3c_v\gamma}{8} + b_1^3b_2(6\mathcal{P} - 9b_2\kappa)\right)\sin^2(2t-x-y) \\
&\quad \left. + b_1^4b_2^3(3b_2\kappa - 4\mathcal{P})\sin^3(2t-x-y) + b_1^4b_2^4\mathcal{P}\sin^4(2t-x-y)\right].
\end{aligned}$$

Periodic boundary conditions are concerned. The initial computational mesh is uniformly divided into $N_x \times N_y$ rectangular cells. Calculating to time $T = 0.1$ with the explicit scheme and the EIN scheme, respectively, we show the error and order in Table 6.1 with different $\kappa = 0.01, 0.1$. Under these parameters $b_1 = 1,\ b_2 = 0.25,\ c_v = 1,\ \mathcal{P} = 10^{-5}$, we do not need a positivity-preserving limiter.

Numerical results show that both of these two schemes achieve second-order accuracy. When κ is not too small, the time step constraint of the diffusion term τ_{diff}^n in (3.21) is more severe than that of the advection term τ_{ad}^n in (3.20). The last two columns in Table 6.1 are the first time step and CPU time cost of these two schemes, and one can see that under $\kappa = 0.1$, the CPU time of the EIN scheme is only about $\frac{1}{10}$ of that of the explicit scheme.

Next, we take $b_1 = 2,\ b_2 = 0.99999,\ c_v = 1,\ \mathcal{P} = 10^{-5},\ \kappa = \frac{10^{-5}}{3}$ to verify our explicit scheme can maintain second-order accuracy with the positivity-preserving limiter. The last column in Table 6.2 represents the percentage of cells modified by the positivity-preserving limiter.

6.2 The non-oscillation tests

6.2.1 The shock tube problem

Here, we compare the EIN scheme and the explicit scheme on the test with the following discontinuous initial condition

$$\rho = 0.001,\ u = v = 0,\ \begin{cases} T = 1, & 0 \le r \le 0.4 \\ T = 10, & 0.4 \le r \le 0.8 \\ T = 0.5, & 0.8 < r \le 1.2 \end{cases} \tag{6.40}$$

and we calculate to time $T = 5 \times 10^{-4}$ with $\gamma = 1.4,\ \mathcal{P} = 10^{-1},\ \kappa = 10^{-2}$ on a quarter of the circular domain $0 \le r \le 1.2$, and symmetric boundary conditions are applied.

In Figure 6.2, we show the computational meshes at $T = 0$, $T = 2.5 \times 10^{-4}$ and $T = 5 \times 10^{-4}$ with 500 cells, respectively. We can observe that the vertices in the middle area move with the shocks in the Lagrangian scheme. From Figure 6.3, we can observe that these two Lagrangian schemes capture the shocks well.

Compared with the explicit scheme, there are some oscillations near the discontinuities produced in the EIN scheme, because we do not apply the WENO reconstruction for the implicit part to handle these oscillations, but the explicit scheme with the WENO reconstruction do not generate such oscillations.

In the meantime, we compare the efficiency of these two schemes. While the explicit scheme costs 297.42 seconds with 2,254 time steps, the EIN scheme costs 7.84 seconds with only 53 time steps which is much more efficient.

6.2.2 The Sedov blast wave problem

We now consider the Sedov blast wave problem on a Cartesian grid $\Omega = [0, 1.2] \times [0, 1.2]$ with initial uniform 1,600 cells. The initial density is set as 1 and the initial velocity is set

Table 6.1: Error and order for the explicit and EIN Lagrangian schemes with $b_1 = 1,\ b_2 = 0.25,\ c_v = 1,\ \mathcal{P} = 10^{-5},\ \gamma = \frac{5}{3}$.

N_x, N_y	L^1 error	order	L^2 error	order	L^∞ error	order	τ^0	CPU time
$\kappa = 0.01$, explicit scheme, $\tau = \min(0.5\tau_{ad}, 0.25\tau_{diff})$								
20	6.9010E-03		8.4434E-03		1.9472E-02		2.28E-01	3.28E-01
40	3.5759E-03	0.95	4.5040E-03	0.91	9.3469E-03	1.06	5.69E-02	1.73E+00
80	9.8376E-04	1.86	1.2566E-03	1.84	2.5619E-03	1.87	1.42E-02	2.27E+01
120	4.3671E-04	2.00	5.5971E-04	1.99	1.1368E-03	2.00	6.30E-03	9.94E+01
160	2.4515E-04	2.01	3.1484E-04	2.00	6.3879E-04	2.00	3.54E-03	3.14E+02
200	1.5708E-04	1.99	2.0205E-04	1.99	4.0950E-04	1.99	2.27E-03	7.52E+02
$\kappa = 0.1$, explicit scheme, $\tau = \min(0.5\tau_{ad}, 0.25\tau_{diff})$								
20	5.9834E-03		7.1400E-03		1.2448E-02		2.28E-02	8.59E-01
40	1.3913E-03	2.10	1.6010E-03	2.16	2.9045E-03	2.10	5.69E-03	1.15E+01
80	3.4063E-04	2.03	3.8476E-04	2.06	7.1093E-04	2.03	1.42E-03	1.76E+02
120	1.5065E-04	2.01	1.6945E-04	2.02	3.1656E-04	2.00	6.30E-04	8.92E+02
160	8.4579E-05	2.01	9.4960E-05	2.01	1.7765E-04	2.01	3.54E-04	2.80E+03
200	5.4055E-05	2.01	6.0655E-05	2.01	1.1299E-04	2.03	2.27E-04	6.77E+03
$\kappa = 0.01$, EIN scheme $a_0 = b_0 = 1$, $\tau = 0.5\tau_{ad}$								
20	5.0349E-03		6.0419E-03		1.3362E-02		1.33E-01	2.03E-01
40	1.4000E-03	1.85	1.8870E-03	1.68	4.9822E-03	1.42	6.65E-02	7.66E-01
80	4.2238E-04	1.73	5.8008E-04	1.70	1.4895E-03	1.74	3.33E-02	1.06E+01
120	1.6655E-04	2.30	2.2870E-04	2.30	5.8331E-04	2.31	2.22E-02	9.31E+01
160	9.9704E-05	1.78	1.3642E-04	1.80	3.4174E-04	1.86	1.67E-02	1.96E+02
200	5.9618E-05	2.30	8.1251E-05	2.32	2.0210E-04	2.35	1.33E-02	5.64E+02
$\kappa = 0.1$, EIN scheme $a_0 = b_0 = 1$, $\tau = 0.5\tau_{ad}$								
20	4.9369E-03		5.8315E-03		1.2799E-02		1.33E-01	2.03E-01
40	1.2735E-03	1.95	1.6848E-03	1.79	4.2901E-03	1.58	6.65E-02	7.66E-01
80	3.6706E-04	1.79	4.8068E-04	1.81	1.1655E-03	1.88	3.33E-02	1.06E+01
120	1.4037E-04	2.37	1.7847E-04	2.44	4.0690E-04	2.60	2.22E-02	9.31E+01
160	8.4065E-05	1.78	1.0381E-04	1.88	2.2636E-04	2.04	1.67E-02	1.96E+02
200	5.0676E-05	2.27	6.2410E-05	2.28	1.4269E-04	2.07	1.33E-02	5.64E+02

Table 6.2: Error and order for the explicit Lagrangian scheme with $b_1 = 2$, $b_2 = 0.99999$, $c_v = 1$, $\mathcal{P} = 10^{-5}$, $\gamma = \frac{5}{3}$, $\kappa = \frac{10^{-5}}{3}$.

N_x, N_y	L^1 error	order	L^2 error	order	L^∞ error	order	Pos(%)
20	6.2927E-03		7.4460E-03		1.2074E-02		60.00
40	1.3904E-03	2.18	1.5975E-03	2.22	2.9008E-03	2.06	20.35
80	3.4000E-04	2.03	3.8211E-04	2.06	6.9334E-04	2.06	5.71
120	1.5040E-04	2.01	1.6799E-04	2.03	3.0145E-04	2.05	1.28
160	8.4460E-05	2.01	9.4037E-05	2.02	1.6714E-04	2.05	0.16
200	5.4019E-05	2.00	6.0013E-05	2.01	1.0578E-04	2.05	0.00

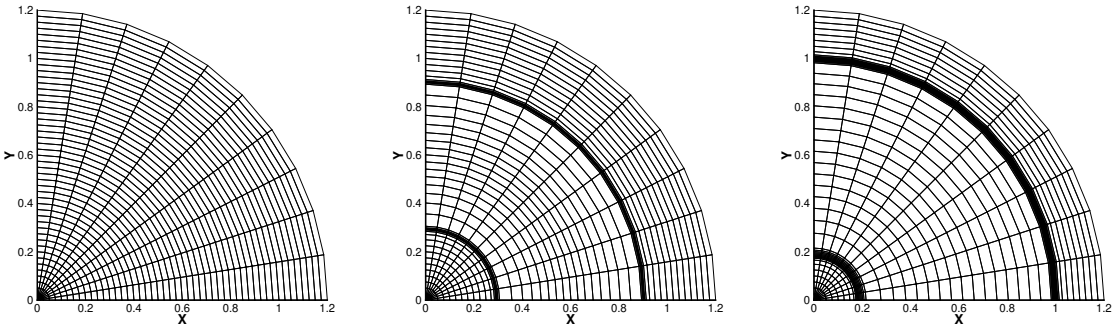

(a) Initial mesh (b) $T = 2.5 \times 10^{-4}$ (c) $T = 5 \times 10^{-4}$

Figure 6.2: Computational meshes of the non-oscillation test at different time.

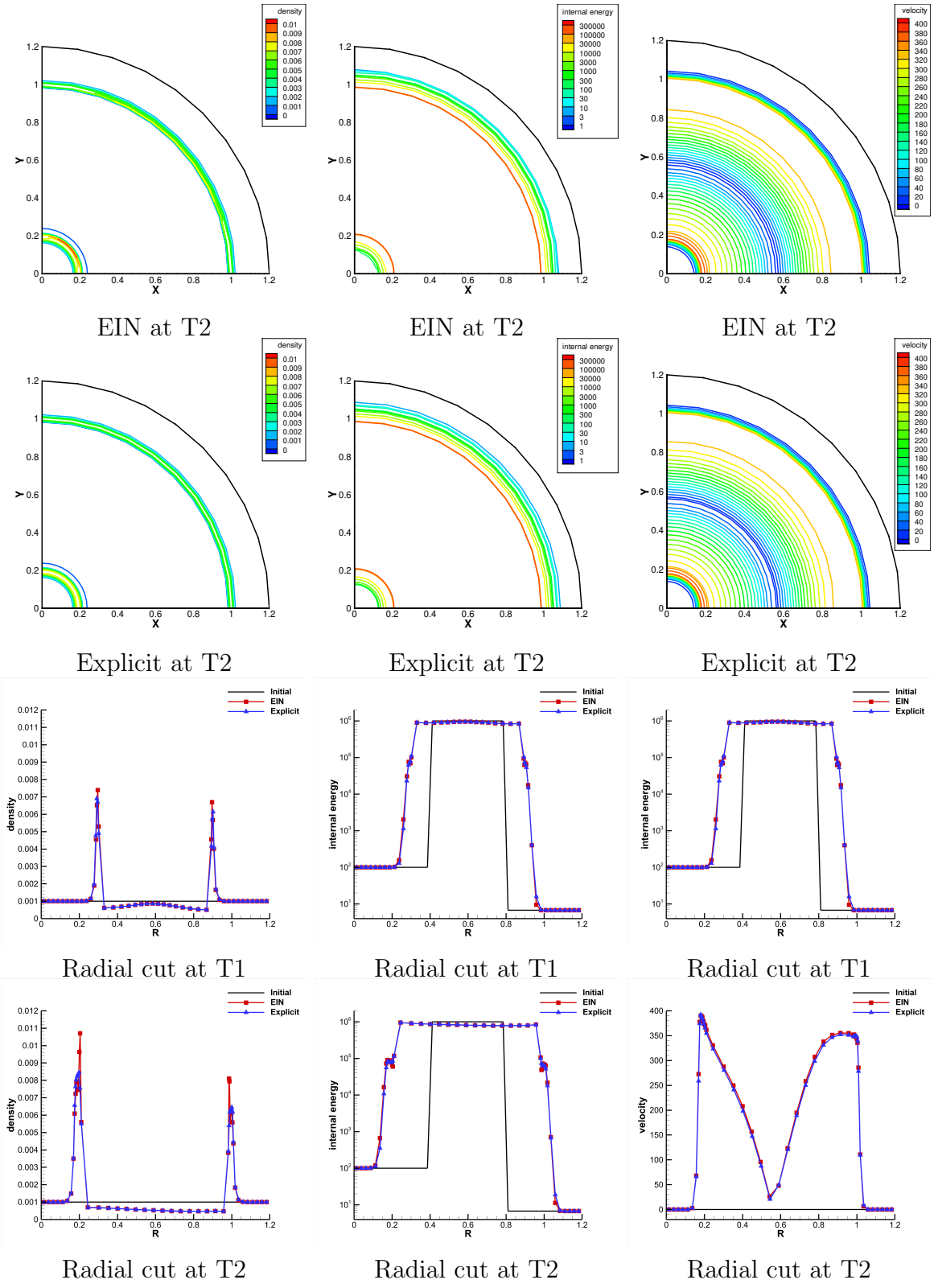

Figure 6.3: Numerical solutions of density (first column), internal energy (second column) and radial velocity (last column) for the non-oscillation test. T1 and T2 represent time $T = 2.5 \times 10^{-4}$ and $T = 5 \times 10^{-4}$, respectively.

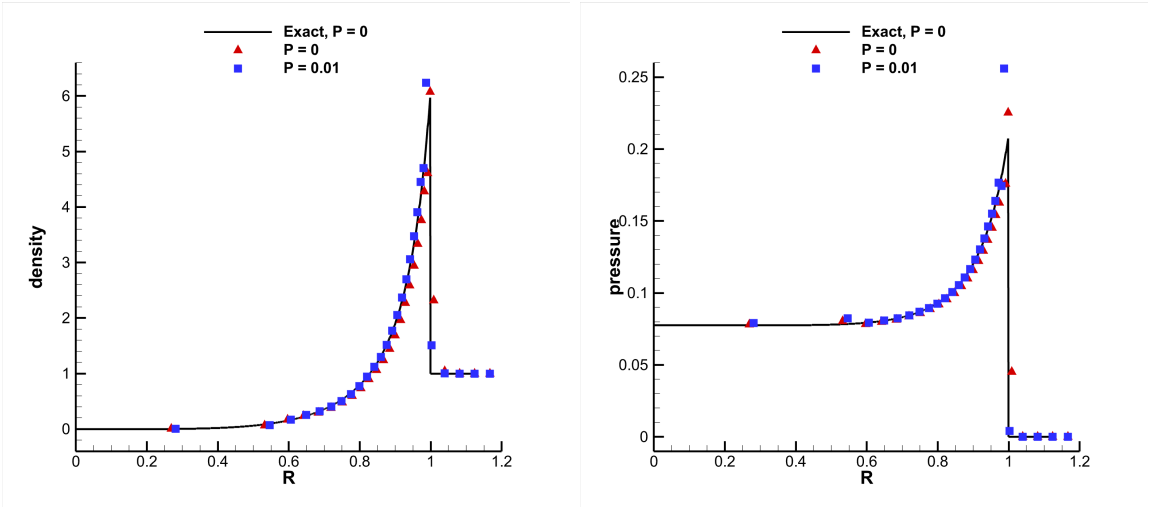

Figure 6.4: Radial cuts of the numerical solutions for the Sedov problem with $\mathcal{P} = 0, 0.01$ and $\kappa = 0$. Here, the exact solutions are under $\mathcal{P} = \kappa = 0$ for the Euler equations.

as 0. The initial internal energy is as 10^{-12} for almost everywhere, except for the only one cell $I_{1,1}$ near the origin which is set as $e^*_{1,1} = \frac{0.244816}{|I_{1,1}|}$. Since the initial internal energy 10^{-12} is very close to 0, the simulation would fail if the positivity-preserving limiter is not used.

In Figure 6.4 and Figure 6.5, we demonstrate the cut lines at $x = y$ for density and total pressure with different parameters $\mathcal{P}, \kappa$. From Figure 6.4, we can see that our high order scheme captures the shock precisely compared with the exact solution with $\mathcal{P} = \kappa = 0$, and the total pressure with a larger radiative parameter $\mathcal{P}$ is a little higher than that of $\mathcal{P} = \kappa = 0$. In Figure 6.6, we show the contours of the density, and we can observe that the shock fronts are very sharp and clear in these Lagrangian schemes. Due to the larger radiation diffusion term, the inner mesh deformation is much less severe with a larger $\kappa = 10^{-2}$ in the right bottom subfigure of Figure 6.6.

6.3 Positivity-preserving test

Now, we consider the performance of our explicit Lagrangian scheme on the positivity-preserving property. The test problem has the following discontinuous initial condition on a

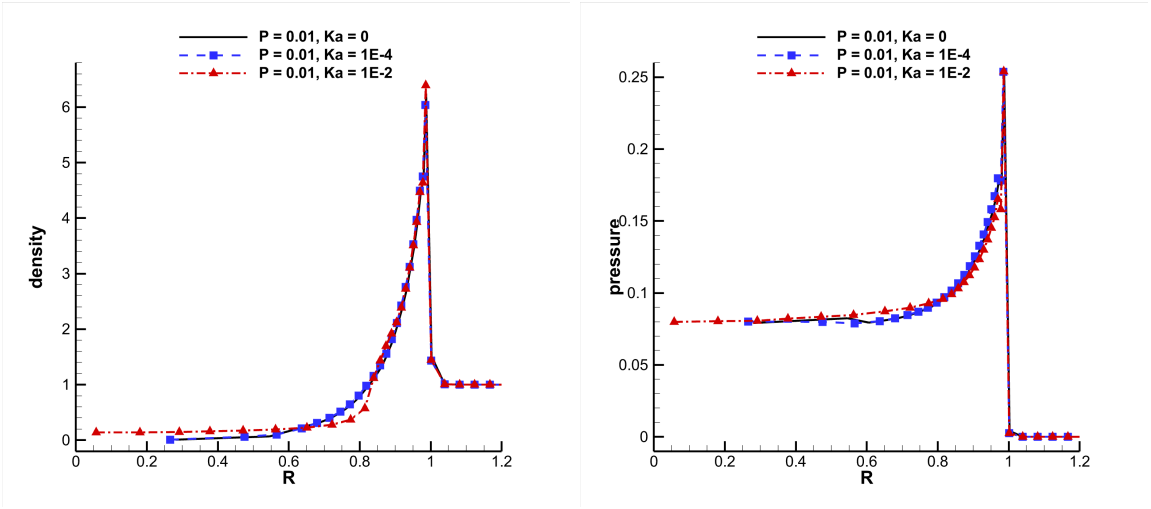

Figure 6.5: Radial cuts of the numerical solutions for the Sedov problem with $\mathcal{P} = 0.01$ and $\kappa = 0, 10^{-4}, 10^{-2}$.

quarter of the circular mesh with the radius $0 \le r \le 12$,

$$\begin{cases} \rho = 1,\ u = v = 0,\ p^* = 0.1, & r \le 3, \\ \rho = 0.001,\ u = v = 0,\ p^* = 10^{-7}, & r > 3. \end{cases} \tag{6.41}$$

We show the radial cuts of the numerical results at time $T = 6$ with different mesh sizes in Figure 6.7. We take $\gamma = \frac{5}{3}$, $c_v = \frac{1}{\gamma(\gamma-1)}$, $\mathcal{P} = 10^{-4}$, $\kappa = 10^{-4}$ in this test. The initial pressure is 10^{-7} which is very close to 0, so the numerical simulation will fail due to the negative pressure if the positivity-preserving limiter is not used. In Figure 6.7, we can observe that our explicit Lagrangian scheme preserves positivity well and there are no numerical oscillations near the discontinuities. Comparing to the reference solution on the fixed denser mesh, the positions of the shock and the contact discontinuity can converge to those of the reference solution. In Figure 6.8, we show the two-dimensional contours of the physical variables with 4,000 cells.

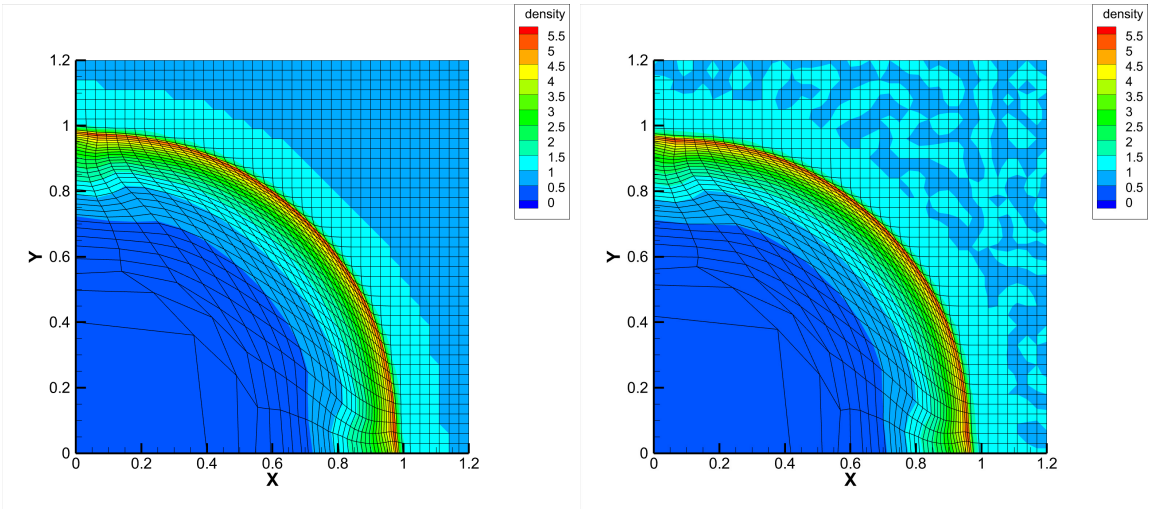

(a) $\mathcal{P} = 0, \kappa = 0$

(b) $\mathcal{P} = 10^{-2}, \kappa = 0$

(c) $\mathcal{P} = 10^{-2}, \kappa = 10^{-4}$

(d) $\mathcal{P} = 10^{-2}, \kappa = 10^{-2}$

Figure 6.6: Numerical solutions of density for the Sedov problem.

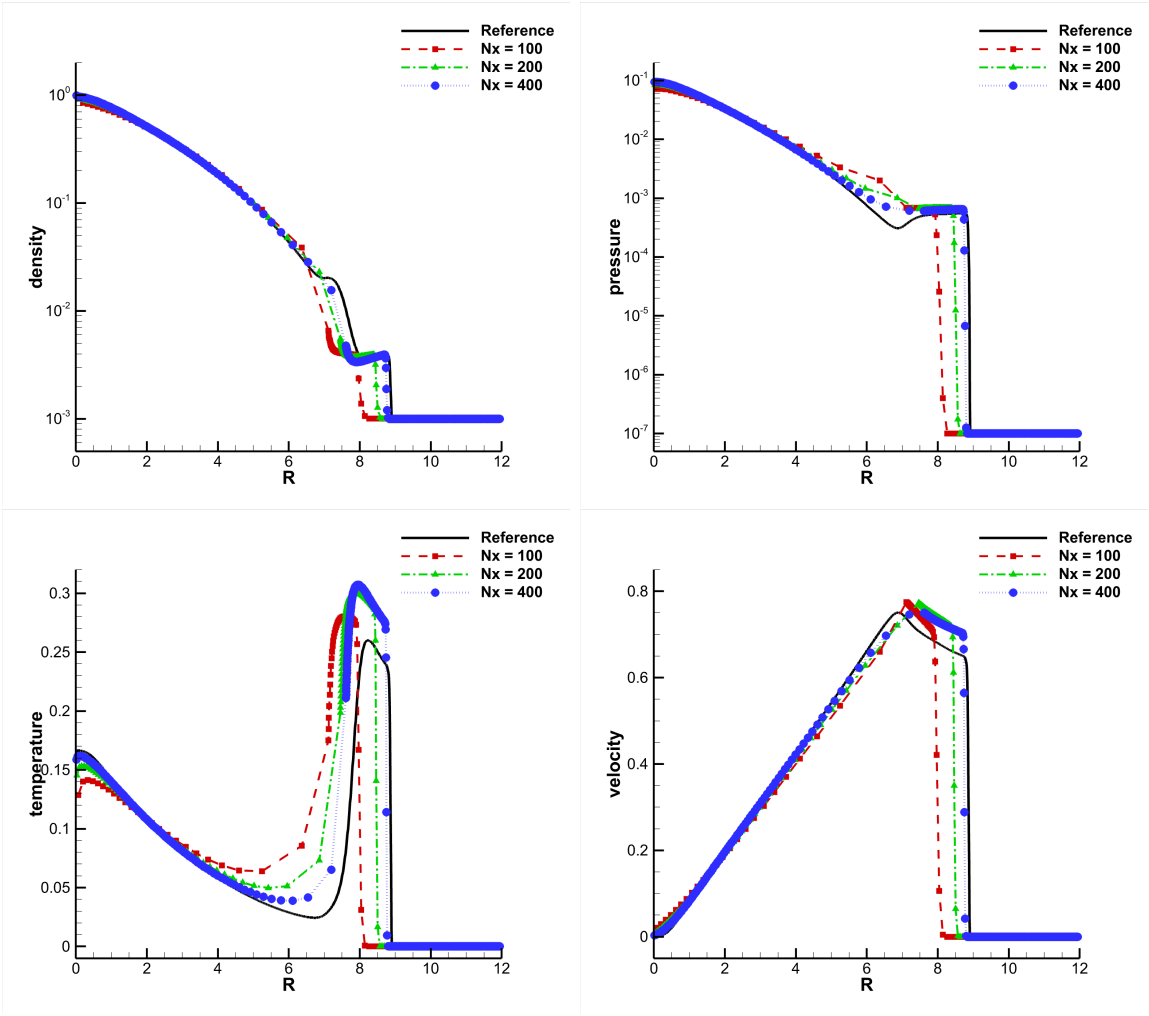

Figure 6.7: Numerical solutions of the explicit Lagrangian scheme for the positivity-preserving test 6.3 at the time $T = 6$ with 1,000, 2,000 and 4,000 cells. N_x means the number of cells on the x direction.

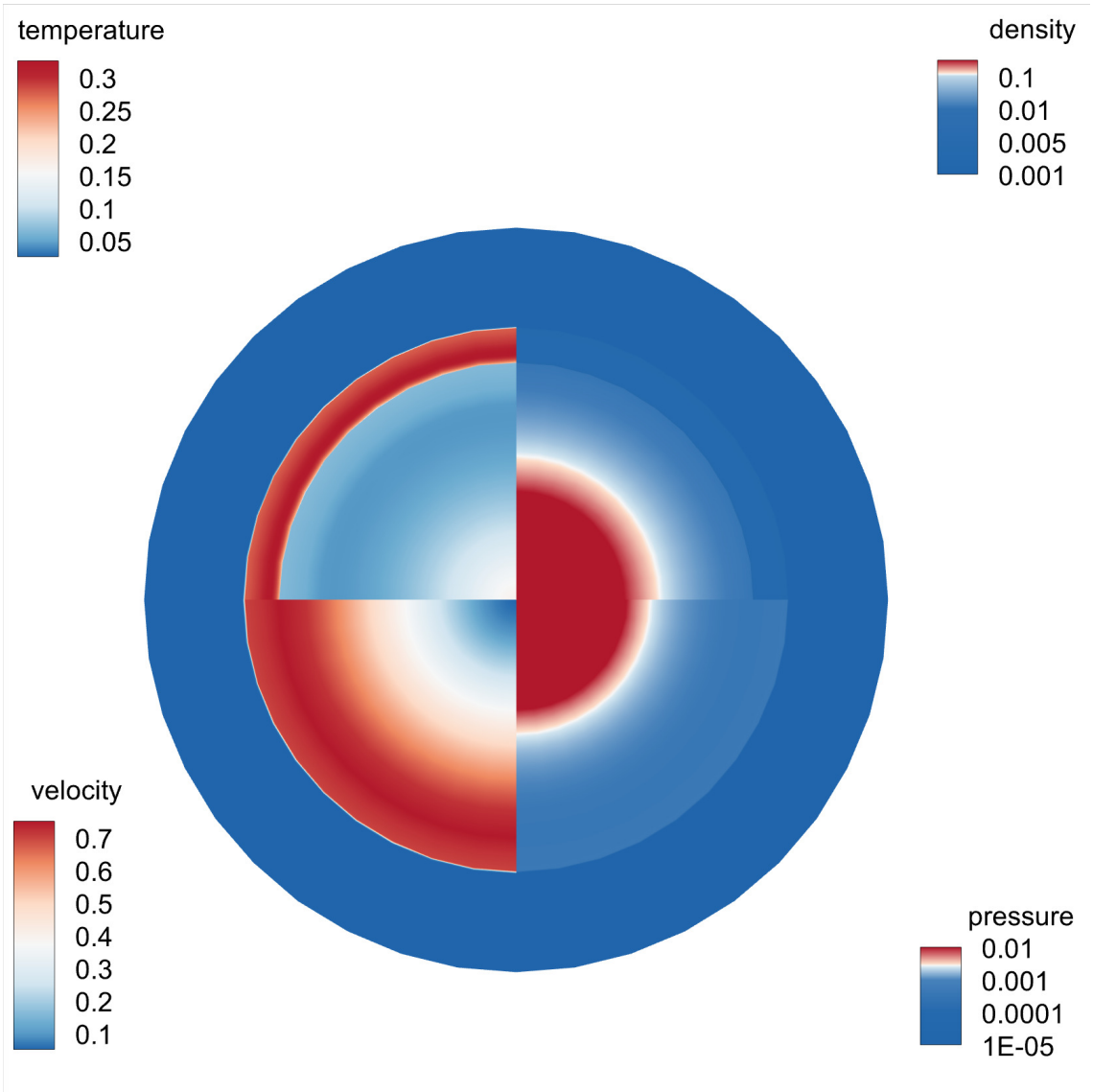

Figure 6.8: Contours of the explicit Lagrangian scheme for the positivity-preserving test 6.3 at the time $T = 6$ with 4,000 cells.

6.4 Multi-material problems

6.4.1 The multi-material radiative shock tube problem

Consider solving (2.1) for the γ-law gas with different initial conditions and γ on different sides of the interface

$$\begin{cases} \rho = 1,\ u = v = 0,\ T = 1.4,\ \gamma = 1.4, & 0 \le r \le 6 \\ \rho = 0.125,\ u = v = 0,\ T = \frac{4}{3},\ \gamma = \frac{5}{3}, & 6 < r \le 12 \end{cases} \tag{6.42}$$

where $c_v = \frac{1}{\gamma(\gamma-1)}$, $\mathcal{P} = \kappa = 10^{-2}$. On different sides of the interface, we have different specific heat capacities of the fluid, which is difficult for the fixed mesh methods to keep a clear interface. We calculate to the time $T = 1.5$, on a quarter of the circular domain with 2,000 cells, and symmetric boundary conditions are applied. In Figure 6.9, we show the radial cuts of the numerical results of density, pressure, temperature and velocity for the explicit Lagrangian scheme with $\kappa = 0, 0.01$, respectively.

Since the vertices in the Lagrangian scheme move with the fluid, it can track the interface automatically, and we can see that the interface is very sharp in Figure 6.9 without oscillations, which verifies the advantages of the Lagrangian scheme and the WENO reconstruction.

6.4.2 The air-water-air problem

Consider the two-fluid flow problem with the initial condition as [19]

$$\begin{cases} \rho = 0.001,\ u = v = 0,\ T = 10^6,\ \gamma = 1.4,\ p_c = 0, & 0 \le r \le 0.2 \\ \rho = 1,\ u = v = 0,\ T = \frac{3001}{35},\ \gamma = 7,\ p_c = 3000, & 0.2 < r \le 1 \\ \rho = 0.001,\ u = v = 0,\ T = 1,\ \gamma = 1.4,\ p_c = 0, & 1 < r \le 1.2 \end{cases} \tag{6.43}$$

and the equation of state for water follows as

$$p = (\gamma - 1)\rho e - \gamma p_c, \quad a = \sqrt{\gamma \frac{p + p_c}{\rho}}.$$

So the conserved variable total energy E^* can be represented by

$$E^* = E + E_r = \frac{1}{2}\rho(u^2 + v^2) + \frac{p + \gamma p_c}{\gamma - 1} + \mathcal{P}T^4.$$

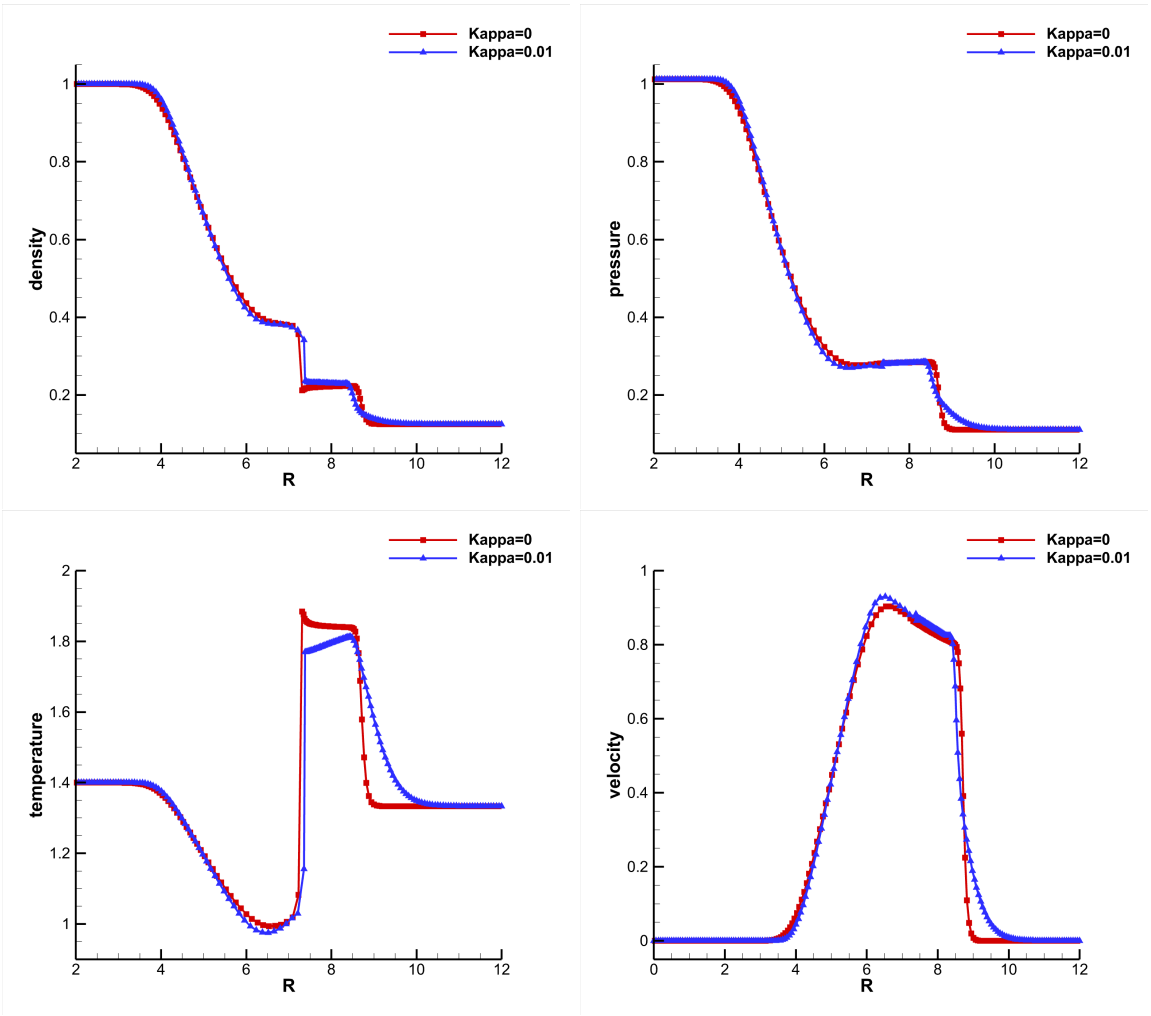

Figure 6.9: Radial cuts of the numerical solutions for the multi-material radiative shock tube problem at time $T = 1.5$ with 2,000 cells.

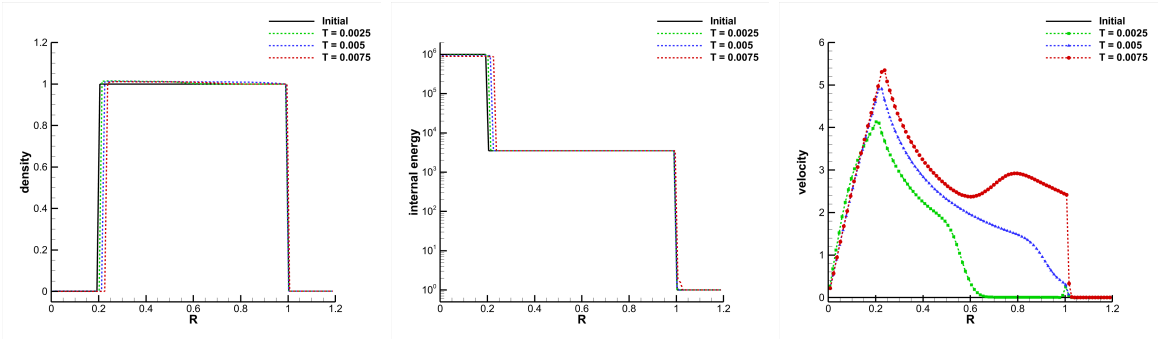

Figure 6.10: Radial cuts of the numerical solutions for the air-water-air problem under the initial condition (6.43) with $\mathcal{P} = \kappa = 0$ at time $T = 0.0025, 0.005, 0.0075$, respectively.

On the other hand, we have $e = c_v T + \frac{p_c}{\rho}$, so E^* can also be represented by the temperature and other physical variables as

$$E^* = \frac{1}{2}\rho(u^2 + v^2) + \rho c_v T + p_c + \mathcal{P}T^4.$$

First, we use the explicit Lagrangian scheme to calculate to the typical time 0.0025, 0.005, 0.0075, respectively, with $\mathcal{P} = \kappa = 0$ and show the radial cuts of the density, internal energy and radial velocity in Figure 6.10 at the different time. In Figure 6.11, we show the contours with 1,000 cells. Our explicit Lagrangian scheme preserves positivity well and keeps high resolution near the discontinuities.

Next, in order to compare the numerical results with $\kappa = 0$ and different radiative parameter $\mathcal{P}$, we take the initial condition as (6.44), and show the radial cuts of the numerical results in Figure 6.12. One can observe that, with the radiation constant $\mathcal{P}$ increasing, the radiation energy $E_r = \mathcal{P}T^4$ will increase and make the radial velocity near the interface decreasing.

$$\begin{cases} \rho = 0.001,\ u = v = 0,\ T = 10,\ \gamma = 1.4,\ p_c = 0, & 0 \le r \le 0.2 \\ \rho = 1,\ u = v = 0,\ T = \frac{3001}{35},\ \gamma = 7,\ p_c = 3000, & 0.2 < r \le 1 \\ \rho = 0.001,\ u = v = 0,\ T = 0.1,\ \gamma = 1.4,\ p_c = 0, & 1 < r \le 1.2 \end{cases} \tag{6.44}$$

Last, we set the same initial total energy for the air and water in (6.45) to compare the numerical results with $\mathcal{P} = 10^{-6}$ and different κ. The numerical results are shown in Figure 6.13. and one can observe that, with the diffusion term parameter κ increasing, the radiation

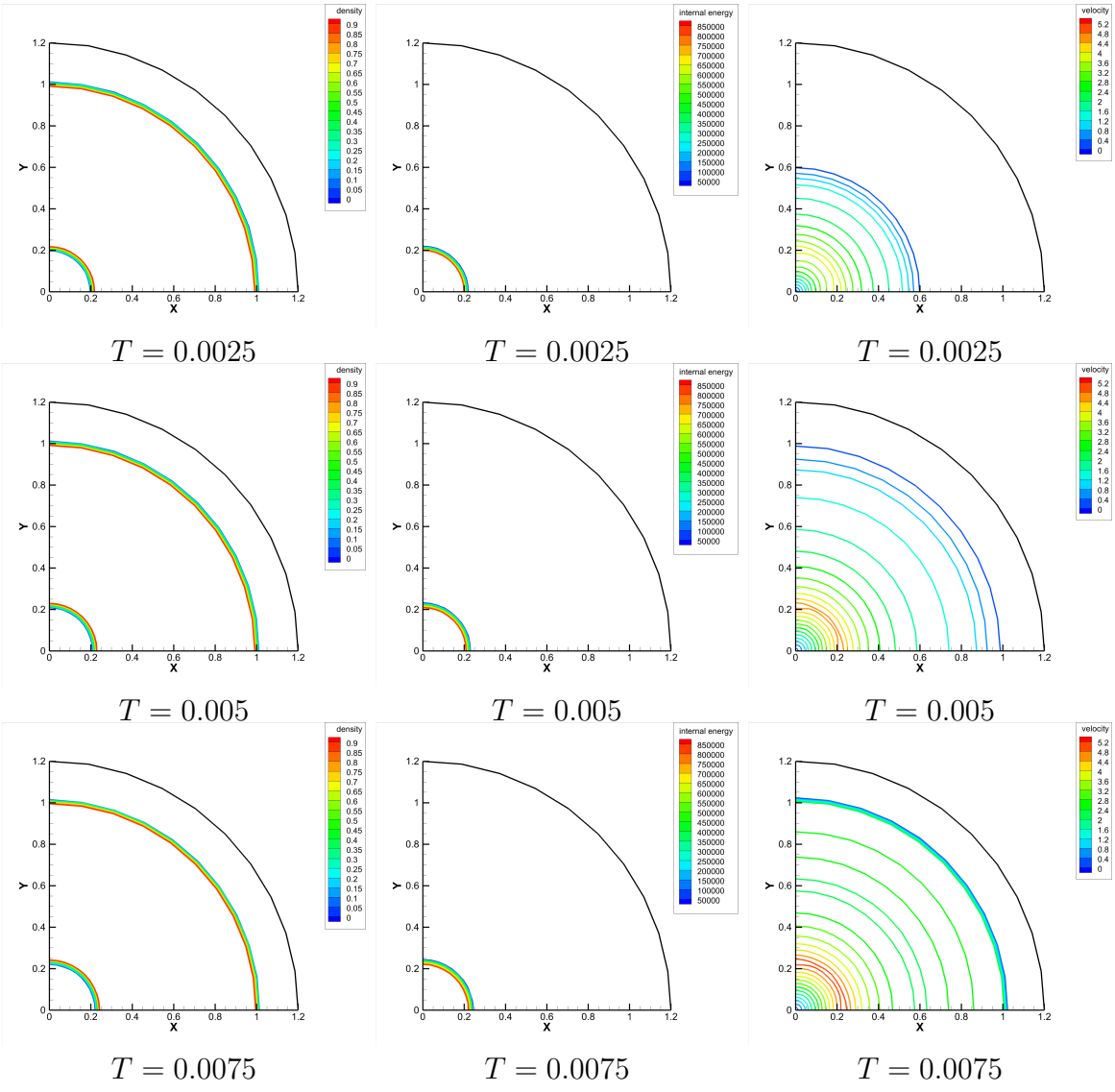

Figure 6.11: Contours of density (first column), internal energy (second column) and radial velocity (last column) for the air-water-air problem under the initial condition (6.43) with $\mathcal{P} = \kappa = 0$ at different time, respectively.

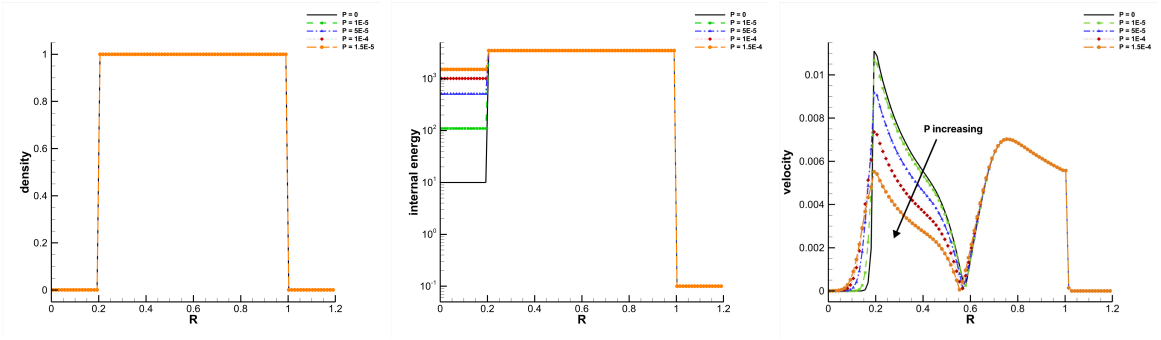

Figure 6.12: Radial cuts of the numerical solutions for the air-water-air problem under the initial condition (6.44) at time $T = 0.0025$ with $\kappa = 0$ and different $\mathcal{P} = 0, 10^{-5}, 5 \times 10^{-5}, 10^{-4}, 1.5 \times 10^{-4}$.

diffusion will play a more important role in RHE and the solution will dissipates near the discontinuities.

$$\begin{cases} \rho = 0.001,\ u = v = 0,\ E^* = \frac{21001}{6},\ \gamma = 1.4,\ p_c = 0, & 0 \le r \le 0.2 \\ \rho = 1,\ u = v = 0,\ E^* = \frac{21001}{6},\ \gamma = 7,\ p_c = 3000, & 0.2 < r \le 1.0 \\ \rho = 0.001,\ u = v = 0,\ E^* = \frac{21001}{6},\ \gamma = 1.4,\ p_c = 0, & 1 < r \le 1.2. \end{cases} \tag{6.45}$$

6.4.3 The ablation test

Referring to [1], we design an ablation test which consists of an outer shell and an inner shell made from deuterium-tritium (DT) ice, with a low-density DT gas. There are four layers of materials in this problem, and ideal gas equation of state is considered. The computational domain is a quarter of the circular domain $0 \le r \le 0.2$ with 2,000 cells. The initial conditions are listed in Table 6.3 and all of the materials' initial velocities are 0.

Table 6.3: Initial conditions for the ablation test.

Material	range	ρ	E^*	γ	c_v
i	$r \in [0, 0.0833]$	0.03	0.592	1.45	1.0000
ii	$r \in (0.0833, 0.0958]$	0.25	1.218	1.45	1.0000
iii	$r \in (0.0958, 0.1125]$	1.08	1.231	1.30	0.1150
iv	$r \in (0.1125, 0.2]$	0.01	15.66	1.67	0.3375

We use the explicit Lagrangian scheme to calculate to the time $T = 0.06$ with $\mathcal{P} = 0.1, \kappa = 10^{-4}$ and show the numerical results at different time in Figure 6.14. Reflective

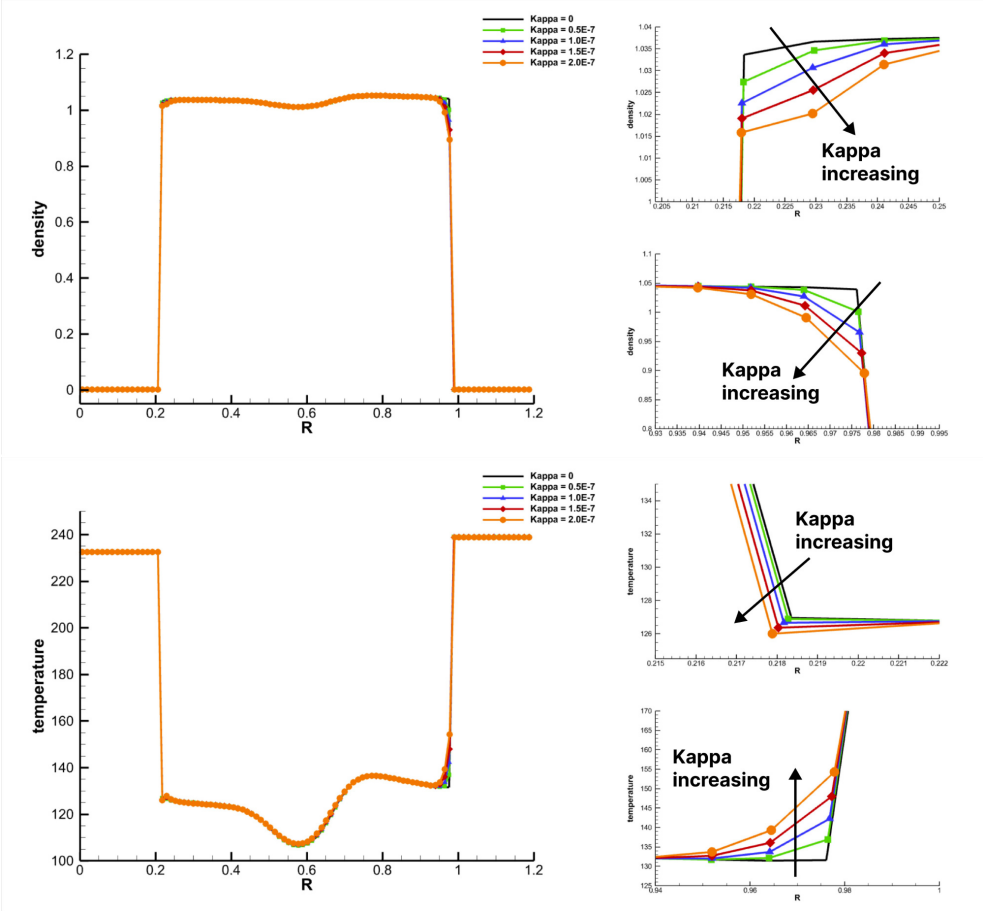

Figure 6.13: Radial cuts of the numerical solutions for the air-water-air problem under the initial condition (6.45) at time $T = 0.002$ with $\mathcal{P} = 10^{-6}$ and different $\kappa = 0, 5 \times 10^{-8}, 10^{-7}, 1.5 \times 10^{-7}, 2 \times 10^{-7}$.

boundary conditions are considered for the left and bottom boundaries, free boundary conditions are considered for the boundaries with $r = 0.2$. From Figure 6.14, we can observe clear material interfaces on the Lagrangian moving meshes. Due to the high temperature and high pressure in the outer layer, the inner DT material layer will be compressed first (see the first two rows in Figure 6.14 at the time $T = 0$ and $T = 0.01$). When the inner pressure is higher than the outer material (see the third row in Figure 6.14 at the time $T = 0.04$), it will expand outward (see the last row in Figure 6.14 at the time $T = 0.06$) until they tend to balance.

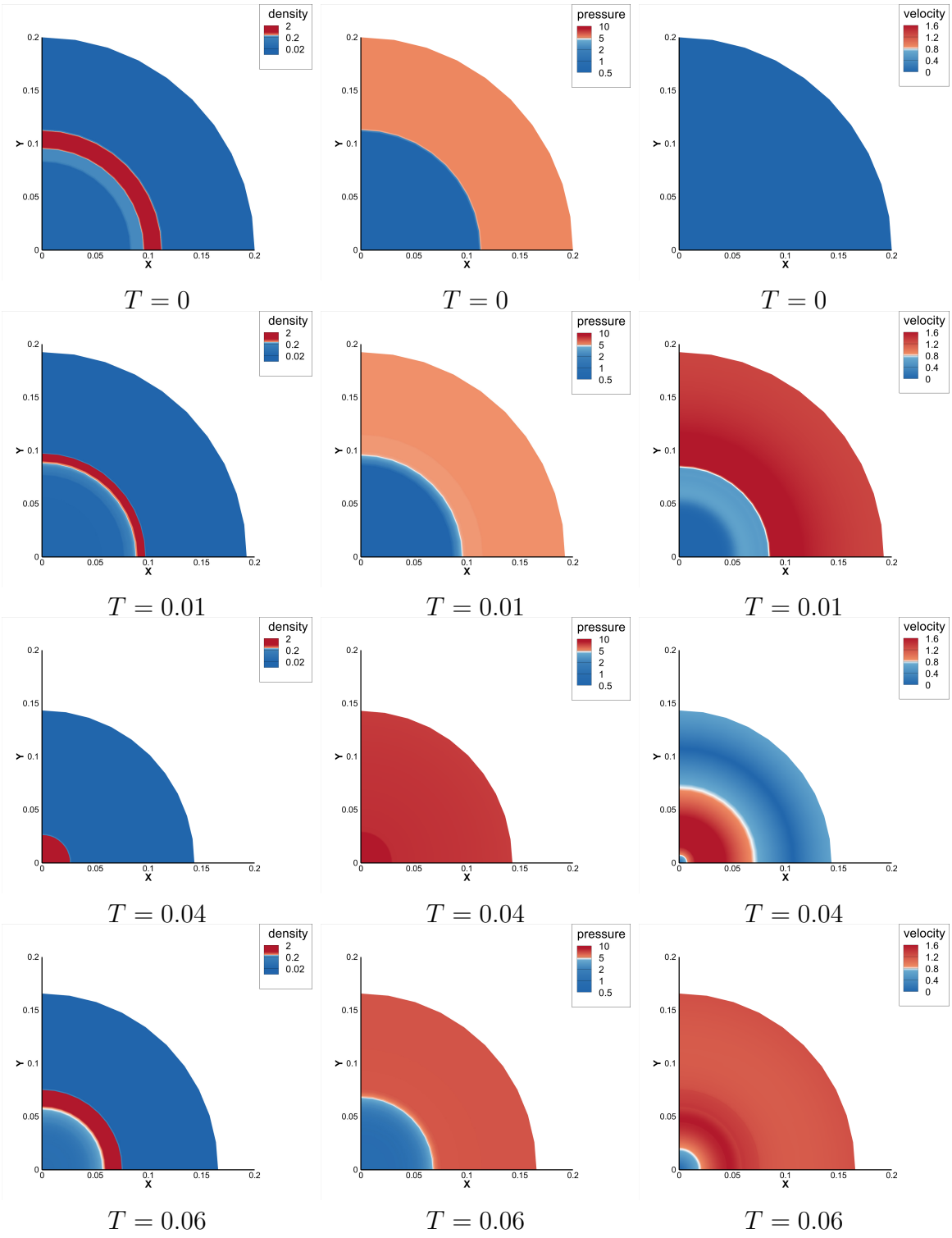

Figure 6.14: Numerical solutions of density (first column), total pressure (second column) and radial velocity (last column) for the ablation problem.

7 Conclusion

This paper presents an extension of the Lagrangian finite volume scheme for RHE in the equilibrium-diffusion limit [7] to the two-dimensional case. High-order Lagrangian schemes are developed using the multi-resolution WENO reconstruction, HLLC numerical flux, and SSP-RK time discretization. To preserve positivity, a positivity-preserving limiter has been added for density and internal energy in the explicit scheme. Numerical experiments verify that the explicit Lagrangian scheme is conservative, high-order accurate, positivity-preserving and non-oscillatory.

To overcome the time step restriction caused by the radiation diffusion term in the explicit scheme, we have developed a high-order explicit-implicit-null (EIN) Lagrangian scheme, which adds a sufficiently large artificial linear diffusion term to both sides of the scheme and then discretize this term on the right-hand side implicitly. This EIN scheme is much more efficient than the explicit scheme, particularly when κ in the diffusion term is not very small, and we verify its accuracy and stability in the simulations.

Due to the use of cells with straight-line edges, our Lagrangian scheme is restricted to second order accuracy, even though the third order reconstructions and time discretization are used [5]. To achieve third or higher order accuracy, curved cells are necessary, which is our future work. The Lagrangian finite volume scheme may become unstable or fail due to the tangled computational mesh when solving the distorted fluid flow in high-dimensional cases. Therefore, implementing this Lagrangian scheme in the arbitrary Lagrangian-Eulerian (ALE) framework using the remapping technique in [13] is also our future work.

A Appendix

A.1 WENO reconstruction for the conserved variables

In the finite volume method, we reconstruct high-order polynomials $\boldsymbol{U}_{i,j}(x,y)$ on each cell $I_{i,j}$ with the information of the cell averages $\bar{\boldsymbol{U}}_{i,j}$ via the multi-resolution WENO reconstruction

[28, 29]. Let us take the cell $I_{i,j}$ and one of the conserved variable $\rho \in \boldsymbol{U} = (\rho, \rho u, \rho v, E^*)^T$ as an example to explain the reconstruction procedure.

1. Reconstruct three different degrees of conserved polynomials $q_1(x,y)$, $q_2(x,y)$, $q_3(x,y)$ satisfying

$$\begin{aligned} \min \sum_{\tilde{I} \in S_l} \left| \int_{\tilde{I}} q_l(x,y) dxdy - \bar{\rho}_{\tilde{I}} |\tilde{I}| \right|^2, \\ \text{s.t.} \int_{I_{i,j}} q_l(x,y) dxdy = \bar{\rho}_{i,j} |I_{i,j}|, \end{aligned} \tag{A.46}$$

   for $l = 1, 2, 3$ on three nested central stencils $S_1 = \{I_{i,j}\}$,

$$S_2 = \{I_{i,j},\ I_{i+1,j},\ I_{i-1,j},\ I_{i,j+1},\ I_{i,j-1}\},$$

   and

$$\begin{aligned} S_3 = \{&I_{i,j},\ I_{i+1,j},\ I_{i-1,j},\ I_{i,j+1},\ I_{i,j-1}, \\ &I_{i+1,j+1},\ I_{i+1,j-1},\ I_{i-1,j+1},\ I_{i-1,j-1}\}, \end{aligned}$$

   respectively. It is obvious that $q_1(x,y) = \bar{\rho}_{i,j}$, and $q_2(x,y), q_3(x,y)$ should be determined by the least square method, and we show these stencils in the left subfigure of Figure A.15.

2. Combine $q_1(x,y)$, $q_2(x,y)$, $q_3(x,y)$ with the linear weights

$$\begin{array}{rcl} p_1(x,y) &=& q_1(x,y) \\ p_2(x,y) &=& \frac{1}{\gamma_{2,2}} q_2(x,y) - \frac{\gamma_{2,1}}{\gamma_{2,2}} p_1(x,y) \\ p_3(x,y) &=& \frac{1}{\gamma_{3,3}} q_3(x,y) - \frac{\gamma_{3,1}}{\gamma_{3,3}} p_1(x,y) - \frac{\gamma_{3,2}}{\gamma_{3,3}} p_2(x,y) \end{array} \tag{A.47}$$

   where $\gamma_{2,1} = \frac{1}{11}$, $\gamma_{2,2} = \frac{10}{11}$ and $\gamma_{3,1} = \frac{1}{111}$, $\gamma_{3,2} = \frac{10}{111}$, $\gamma_{3,3} = \frac{100}{111}$, which makes $\sum_{l=1}^{3} \gamma_{3,l} p_l(x,y) = q_3(x,y)$. The choice of the linear weights follows the suggestion in [28, 29].

3. Calculate the smoothness indicator

$$\beta_l := \sum_{s=1}^{2} \int_{I_{i,j}} |I_{i,j}|^{s-1} \left(\frac{\partial^s}{\partial x^{s_1} \partial y^{s_2}} p_l(x,y) \right)^2 dxdy, \quad s_1 + s_2 = s,\ s_1 \geq 0,\ s_2 \geq 0$$

for $l = 2, 3$. The smoothness indicator β_1 for the zero degree polynomial $p_1(x, y)$ is defined in another way [28],

$$\eta_1 = (\bar{\rho}_{i,j} - \bar{\rho}_{i-1,j})^2,\ \eta_2 = (\bar{\rho}_{i,j} - \bar{\rho}_{i,j+1})^2, \eta_3 = (\bar{\rho}_{i,j} - \bar{\rho}_{i+1,j})^2,\ \eta_4 = (\bar{\rho}_{i,j} - \bar{\rho}_{i,j-1})^2,$$

and β_1 follows

$$\beta_1 = \min\{\eta_1 + \eta_2, \eta_2 + \eta_3, \eta_3 + \eta_4, \eta_4 + \eta_1\}.$$

4. Compute the nonlinear weights ω_1, ω_2, ω_3 with

$$\tau = \left(\frac{|\beta_3 - \beta_1| + |\beta_3 - \beta_2|}{2}\right)^2,\ \bar{\omega}_l = \gamma_{3,l}\left(1 + \frac{\tau}{\beta_l + \varepsilon}\right),\ \omega_l = \frac{\bar{\omega}_l}{\sum_{s=1}^{3} \bar{\omega}_s},\ l = 1, 2, 3$$

here ε is chosen as 10^{-6} to avoid zero in denominator. The final reconstruction polynomial for u is defined as

$$\rho_{i,j}(x, y) = \omega_1 p_1(x, y) + \omega_2 p_2(x, y) + \omega_3 p_3(x, y).$$

We could follow this way to reconstruct polynomials for the other conserved variables and obtain the final high order reconstruction polynomial $\boldsymbol{U}_{i,j}(x, y)$.

A.2 WENO reconstruction for the derivative variables

When it comes to the derivatives $\partial_x T^4$ and $\partial_y T^4$, in the diffusion term, we should perform another WENO reconstruction procedure for the derivative variables $\partial_x \boldsymbol{U}$, $\partial_y \boldsymbol{U}$. Here, we reconstruct polynomials on each edge of the cell and all of the stencils should contain two adjacent cells of the edge. For example, if we need to perform reconstruction on the right edge of the cell $I_{i,j}$ marked in red in Figure A.15 and Figure A.16, then the stencils should contain $I_{i,j}$ and $I_{i+1,j}$.

Therefore, define two small stencils $S_{2,1}^{\text{der}}$ and $S_{2,2}^{\text{der}}$ to reconstruct second-order polynomials $q_{2,1}^{\text{der}}(x, y)$ and $q_{2,2}^{\text{der}}(x, y)$,

$$\begin{aligned} S_{2,1}^{\text{der}} &= \{\mathbf{I_{i,j}},\ \mathbf{I_{i+1,j}}, I_{i,j+1}, I_{i,j-1}, I_{i-1,j}\} \\ S_{2,2}^{\text{der}} &= \{\mathbf{I_{i,j}},\ \mathbf{I_{i+1,j}}, I_{i+1,j+1}, I_{i+1,j-1}, I_{i+2,j}\} \end{aligned}$$

which are shown with black and gray quadrilaterals in Figure A.16. The third-order polynomial $q_3^{\rm der}(x,y)$ is reconstructed on the big stencil $S_3^{\rm der}$ in the right subfigure of Figure A.15,

$$S_3^{\rm der} = \{\mathbf{I_{i,j}},\ \mathbf{I_{i+1,j}},\ I_{i-1,j},\ I_{i+2,j},\ I_{i,j+1},\ I_{i+1,j+1},\ I_{i,j-1},\ I_{i+1,j-1}\}.$$

Now, we will introduce the WENO reconstruction procedure for the derivative variables $\partial_x\rho, \partial_y\rho$ at the common edge l^m of $I_{i,j}$ and $I_{i+1,j}$, where $\rho \in \boldsymbol{U}$ is the conserved variable.

1. Reconstruct linear polynomials $q_{2,1}^{\rm der}(x,y)$ and $q_{2,2}^{\rm der}(x,y)$ for the conserved variable on the stencils $S_{2,1}^{\rm der}$ and $S_{2,2}^{\rm der}$, respectively,

$$\begin{aligned} &\min \sum_{\tilde{I}\in S_{2,l}^{\rm der}} \left| \int_{\tilde{I}} q_{2,l}^{\rm der}(x,y)dxdy - \bar{\rho}_{\tilde{I}}|\tilde{I}| \right|^2, \quad l = 1,2 \\ &\text{s.t.} \int_{I_{i,j}} q_{2,l}^{\rm der}(x,y)dxdy = \bar{\rho}_{i,j}|I_{i,j}|, \quad \int_{I_{i+1,j}} q_{2,l}^{\rm der}(x,y)dxdy = \bar{\rho}_{i+1,j}|I_{i+1,j}|, \end{aligned} \tag{A.48}$$

   Reconstruct the quadratic polynomial $q_3^{\rm der}(x,y)$ on the big stencil $S_3^{\rm der}$,

$$\begin{aligned} &\min \sum_{\tilde{I}\in S_3^{\rm der}} \left| \int_{\tilde{I}} q_3^{\rm der}(x,y)dxdy - \bar{\rho}_{\tilde{I}}|\tilde{I}| \right|^2 \\ &\text{s.t.} \int_{I_{i,j}} q_3^{\rm der}(x,y)dxdy = \bar{\rho}_{i,j}|I_{i,j}|, \quad \int_{I_{i+1,j}} q_3^{\rm der}(x,y)dxdy = \bar{\rho}_{i+1,j}|I_{i+1,j}|. \end{aligned} \tag{A.49}$$

2. Combine $q_{2,1}^{\rm der}(x,y),\ q_{2,2}^{\rm der}(x,y),\ q_3^{\rm der}(x,y)$ with the linear weights

$$\begin{aligned} p_{2,1}^{\rm der}(x,y) &= q_{2,1}^{\rm der}(x,y), \quad p_{2,2}^{\rm der}(x,y) = q_{2,2}^{\rm der}(x,y) \\ p_3^{\rm der}(x,y) &= \frac{1}{\gamma_{3,3}} q_3^{\rm der}(x,y) - \frac{\gamma_{3,1}}{\gamma_{3,3}} p_{2,1}^{\rm der}(x,y) - \frac{\gamma_{3,2}}{\gamma_{3,3}} p_{2,2}^{\rm der}(x,y) \end{aligned}$$

   where $\gamma_{3,1} = \gamma_{3,2} = \frac{1}{12},\ \gamma_{3,3} = \frac{10}{12}$, which makes $\gamma_{3,1}p_{2,1}^{\rm der}(x,y)+\gamma_{3,2}p_{2,2}^{\rm der}(x,y)+\gamma_{3,3}p_3^{\rm der}(x,y) = q_3^{\rm der}(x,y)$.

3. Calculate the smoothness indicators from the second order derivatives

$$\beta_3 := \int_{I_{i,j}} |I_{i,j}| \left(\frac{\partial^2}{\partial x^{s_1}\partial y^{s_2}} p_3^{\rm der}(x,y) \right)^2 dxdy,\ s_1+s_2 = 2,\ s_1, s_2 \geq 0.$$

It should be noted that, if we follow this way to define smoothness indicators for $p_{2,1}^{\mathrm{der}}(x,y)$, $p_{2,2}^{\mathrm{der}}(x,y)$, then they will be 0, since they are linear polynomials. Here, to determine β_1, β_2, we will reconstruct two quadratic polynomials $\tilde{p}_{2,1}^{\mathrm{der}}(x,y)$, $\tilde{p}_{2,2}^{\mathrm{der}}(x,y)$ on bigger stencils $\tilde{S}_{2,1}^{\mathrm{der}}$, $\tilde{S}_{2,2}^{\mathrm{der}}$ consisting of 9 cells and covering the stencils $S_{2,1}^{\mathrm{der}}$, $S_{2,2}^{\mathrm{der}}$, respectively. In Figure A.16, we have marked the stencils $\tilde{S}_{2,1}^{\mathrm{der}}$, $\tilde{S}_{2,2}^{\mathrm{der}}$ in the blue dash dot lines. Then, define the smoothness indicators β_1, β_2 as

$$\beta_l := \int_{I_{i,j}} |I_{i,j}| \left(\frac{\partial^2}{\partial x^{s_1} \partial y^{s_2}} \tilde{p}_{2,l}^{\mathrm{der}}(x,y) \right)^2 dxdy, \quad s_1 + s_2 = 2,\ s_1, s_2 \geq 0$$

with $l = 1, 2$.

4. Compute the nonlinear weights ω_1, ω_2, ω_3 with

$$\tau = \left(\frac{|\beta_3 - \beta_1| + |\beta_3 - \beta_2|}{2} \right)^2,\ \bar{\omega}_l = \gamma_{3,l} \left(1 + \frac{\tau}{\beta_l + \varepsilon} \right),\ \omega_l = \frac{\bar{\omega}_l}{\sum_{s=1}^{3} \bar{\omega}_s}.$$

Here, ε is chosen as 10^{-6} to avoid zero in denominator. Final reconstruction polynomial is defined as

$$\rho_{i,j}^m(x,y) = \omega_1 p_{2,1}^{\mathrm{der}}(x,y) + \omega_2 p_{2,2}^{\mathrm{der}}(x,y) + \omega_3 p_3^{\mathrm{der}}(x,y),$$

which is also the reconstruction polynomial for the left edge of the cell $I_{i+1,j}$.

We could follow this way to reconstruct polynomials for the other conserved variables and obtain the final high order reconstruction polynomial $\boldsymbol{U}_{i,j}^m(x,y)$. Then, we can use these polynomials $\boldsymbol{U}_{i,j}^m(x,y)$ to calculate values of the conserved variables and their derivatives $\boldsymbol{U}_{i,j}^m(x,y)$, $\partial_x \boldsymbol{U}_{i,j}^m(x,y)$, $\partial_y \boldsymbol{U}_{i,j}^m(x,y)$ for $\partial_x T^4(\boldsymbol{U}_{i,j}^m)$, $\partial_y T^4(\boldsymbol{U}_{i,j}^m)$ in the diffusion numerical flux. Precisely, we calculate the partial derivatives of T by the formula (2.2),

$$\begin{aligned}
\partial_x \left(T^4 + c_1 T + c_2\right) &= 0 \\
4T^3 T_x + c_1 T_x + T\partial_x c_1 + \partial_x c_2 &= 0 \\
\left(4T^3 + c_1\right) T_x &= -\partial_x c_2 - T\partial_x c_1 \\
\left(4T^3 + c_1\right) T_x &= \tfrac{1}{\mathcal{P}} \left(E_x^* - u(\rho u)_x - v(\rho v)_x + (\tfrac{u^2}{2} + \tfrac{v^2}{2})\rho_x - \rho_x c_v T \right) \\
T_x &= \tfrac{1}{\rho c_v + 4\mathcal{P}T^3} \left(E_x^* - u(\rho u)_x - v(\rho v)_x + \rho_x (\tfrac{u^2}{2} + \tfrac{v^2}{2}) - \rho_x c_v T \right).
\end{aligned}$$

In the same way, we have

$$T_y = \frac{1}{\rho c_v + 4\mathcal{P}T^3} \left(E_y^* - u(\rho u)_y - v(\rho v)_y + \rho_y (\frac{u^2}{2} + \frac{v^2}{2}) - \rho_y c_v T \right).$$

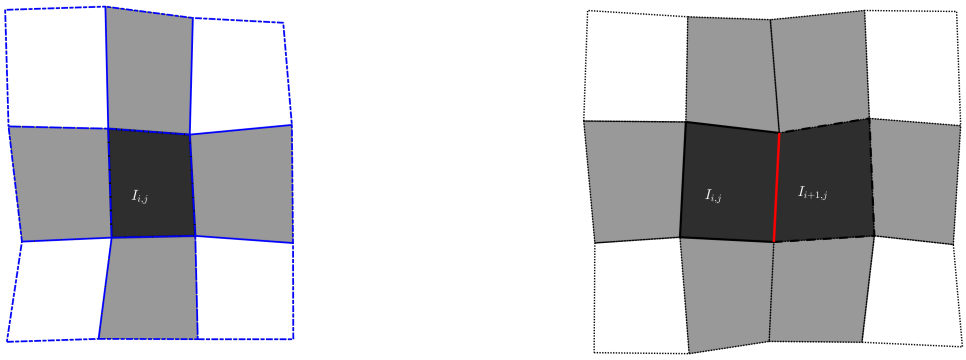

Figure A.15: Left: stencils for the WENO reconstruction for the advection term. The central black quadrilateral is the cell $I_{i,j}$, gray quadrilaterals cells consist of the small stencil S_2, all of nine quadrilaterals cells consist of the big stencil S_3. Right: stencil S_3^{der} for the polynomial $q_3^{\text{der}}(x,y)$. Red line is the common edge and black quadrilaterals are the cells $I_{i,j},\ I_{i+1,j}$.

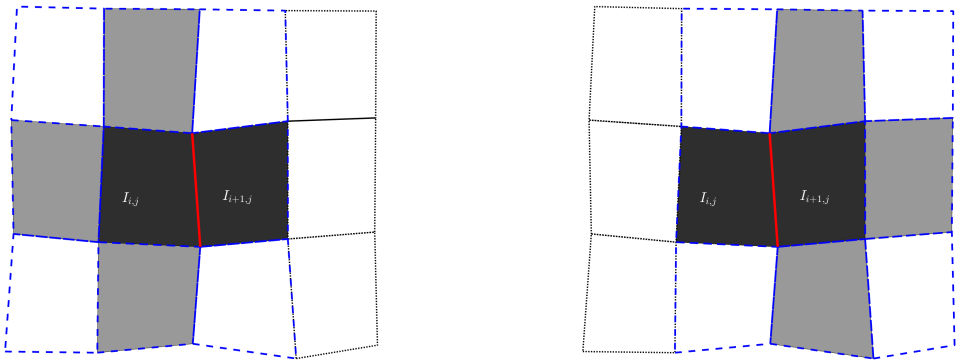

Figure A.16: Stencils for the linear polynomials $q_{2,1}^{\text{der}}(x,y),\ q_{2,2}^{\text{der}}(x,y)$. Red line is the common edge, black quadrilaterals are the cells $I_{i,j},\ I_{i+1,j}$, gray quadrilaterals are the cells in the small stencils $S_{2,1}^{\text{der}},\ S_{2,2}^{\text{der}}$. The nine cells enclosed with blue dash lines are the stencils $\tilde{S}_{2,1}^{der}$ and $\tilde{S}_{2,2}^{der}$.

A.3 Reconstruct polynomials for the artificial diffusion term

In the first order EIN scheme (5.37), for the values $\boldsymbol{U}^{n+1}(x_\alpha^m, y_\alpha^m)$ in $\widehat{\boldsymbol{H}}^{n+1}$ at the time level t^{n+1}, we take the conservative quadratic polynomial $W_{i,j}^{n+1}(x,y)$ for total energy E^* over $I_{i,j}$ as an example to show the specific reconstruction procedure. The stencil of the reconstruction procedure will be set as $I_{i,j}$ and its 8 neighbor cells. Define

$$W_{i,j}^{n+1}(x,y) := a_1^{i,j}+a_2^{i,j}(x-x_{i,j}^c)+a_3^{i,j}(y-y_{i,j}^c)+a_4^{i,j}(x-x_{i,j}^c)^2+a_5^{i,j}(x-x_{i,j}^c)(y-y_{i,j}^c)+a_6^{i,j}(y-y_{i,j}^c)^2,$$

which satisfies

$$\begin{aligned} \min \sum_{I_s^{n+1}\in S_{Ne}^{n+1}} \left| \int_{I_s^{n+1}} W_{i,j}^{n+1}(x,y)dxdy - \bar{E}_{I_s^{n+1}}^{*,n+1}|I_s^{n+1}| \right|^2 \\ \text{s.t.} \int_{I_{i,j}^{n+1}} W_{i,j}^{n+1}(x,y)dxdy = \bar{E}_{i,j}^{*,n+1}|I_{i,j}^{n+1}| \end{aligned} \tag{A.50}$$

where $(x_{i,j}^c, y_{i,j}^c)$ is the centroid of $I_{i,j}^{n+1}$, and S_{Ne}^{n+1} is the set of 8 neighboring cells of $I_{i,j}^{n+1}$, so $I_s^{n+1} \in S_{Ne}^{n+1}$ for $s = 1, \cdots, 8$. Use the same notation in (4.28), the integral becomes

$$\int_{I_s^{n+1}} W_{i,j}^{n+1}(x,y)dxdy = \sum_{\alpha,\beta=1}^{K} \tilde{\omega}_{\alpha,\beta}|J|_s^{\alpha,\beta} W_{i,j}^{n+1}(x_s^{\alpha,\beta}, y_s^{\alpha,\beta}), \quad I_s^{n+1} \in S_{Ne}^{n+1},$$

where $\tilde{\omega}_{\alpha,\beta}$, $|J|_s^{\alpha,\beta}$ are unrelated to $\bar{\boldsymbol{U}}^{n+1}$ and

$$\begin{aligned} W_{i,j}^{n+1}(x_s^{\alpha,\beta}, y_s^{\alpha,\beta}) = \;& W_{i,j}^{n+1}(\mathcal{B}_s(\xi_\alpha, \eta_\beta)) \\ = \;& a_1^{i,j} + a_2^{i,j}(x_s^{\alpha,\beta} - x_{i,j}^c) + a_3^{i,j}(y_s^{\alpha,\beta} - y_{i,j}^c) \\ & + a_4^{i,j}(x_s^{\alpha,\beta} - x_{i,j}^c)^2 + a_5^{i,j}(x_s^{\alpha,\beta} - x_{i,j}^c)(y_s^{\alpha,\beta} - y_{i,j}^c) + a_6^{i,j}(y_s^{\alpha,\beta} - y_{i,j}^c)^2. \end{aligned}$$

Therefore, the integral over cell I_s^{n+1} could be represented as

$$\int_{I_s^{n+1}} W_{i,j}^{n+1}(x,y)dxdy = \boldsymbol{c}_s \boldsymbol{a}_{i,j},$$

here, $\boldsymbol{a}_{i,j} = (a_1^{i,j}, a_2^{i,j}, a_3^{i,j}, a_4^{i,j}, a_5^{i,j}, a_6^{i,j})^T$ are the coefficients in $W_{i,j}^{n+1}(x,y)$ and 1×6 vector $\boldsymbol{c}_s$ only relates with the mesh information and the quadrature weights. We also have the integral over cell $I_{i,j}^{n+1}$ as

$$\int_{I_{i,j}^{n+1}} W_{i,j}^{n+1}(x,y)dxdy = \boldsymbol{c}_{i,j} \boldsymbol{a}_{i,j},$$

where $\boldsymbol{c}_{i,j}$ is a 1×6 vector.

Once we input the mesh information $\Omega = \{I_{i,j}^{n+1}\}_{i,j=1}^{N_x,N_y}$, the above constrained least square problem is equivalent to the following linear system

$$\begin{pmatrix} B^TB & -A^T \\ -A & O \end{pmatrix} \begin{pmatrix} \boldsymbol{a} \\ \lambda \end{pmatrix} = \begin{pmatrix} B^T\boldsymbol{f} \\ -b \end{pmatrix} \tag{A.51}$$

where B is a 8×6 matrix consisting of 8 vectors $\boldsymbol{c}_s$, A is a 1×6 vector $\boldsymbol{c}_{i,j}$, $b = \bar{E}_{i,j}^{*,n+1}$ and the right-hand side $\boldsymbol{f}$ is a 8×1 vector of cell averages $\bar{E}_s^{*,n+1}$ for $s = 1, \cdots, 8$. To be more concise, we omit the cell index i, j here. In the EIN scheme, A and B are known and only depend on the mesh information, but the values of the righthand side $\boldsymbol{f}, b$ are unknown.

In practice, we will take unit vectors

$$\boldsymbol{f}_s = (0, \ \ 0 \ \ \cdots \ \ \underset{\substack{\uparrow \\ s}}{1}, \ \ 0 \ \ \cdots \ \ 0)^T, \quad s = 1 \cdots 8$$

to solve the linear system, and $\boldsymbol{a}$ is the combination of the solutions. In detail, suppose the inverse of $\mathcal{A} := \begin{pmatrix} B^TB & -A^T \\ -A & O \end{pmatrix}$ exists, and we have

$$\begin{pmatrix} \boldsymbol{a} \\ \lambda \end{pmatrix} = \mathcal{A}^{-1} \begin{pmatrix} B^T\boldsymbol{f} \\ b \end{pmatrix}$$

then we obtain

$$\begin{pmatrix} \boldsymbol{a}_0 \\ \lambda_0 \end{pmatrix} = \mathcal{A}^{-1} \begin{pmatrix} \boldsymbol{0} \\ 1 \end{pmatrix}, \quad \begin{pmatrix} \boldsymbol{a}_s \\ \lambda_s \end{pmatrix} = \mathcal{A}^{-1} \begin{pmatrix} B^T\boldsymbol{f}_s \\ 0 \end{pmatrix}, \quad \boldsymbol{f}_s = (0, 0 \cdots 1, 0 \cdots 0)^T$$

where $s = 1, \cdots, 8$. Notice that $\boldsymbol{f} = \sum_{s=1}^{8} \bar{E}_s^{*,n+1}\boldsymbol{f}_s$ and the parameters $\boldsymbol{a}$ follow as

$$\begin{aligned} \begin{pmatrix} \boldsymbol{a} \\ \lambda \end{pmatrix} &= \bar{E}_{i,j}^{*,n+1} \begin{pmatrix} \boldsymbol{a}_0 \\ \lambda_0 \end{pmatrix} + \sum_{s=1}^{8} \bar{E}_s^{*,n+1} \begin{pmatrix} \boldsymbol{a}_s \\ \lambda_s \end{pmatrix} \\ &= \mathcal{A}^{-1} \begin{pmatrix} \boldsymbol{0} \\ \bar{E}_{i,j}^{*,n+1} \end{pmatrix} + \sum_{s=1}^{8} \mathcal{A}^{-1} \begin{pmatrix} B^T\bar{E}_s^{*,n+1}\boldsymbol{f}_s \\ 0 \end{pmatrix} \\ &= \mathcal{A}^{-1} \begin{pmatrix} \boldsymbol{0} \\ \bar{E}_{i,j}^{*,n+1} \end{pmatrix} + \mathcal{A}^{-1} \begin{pmatrix} B^T\sum_{s=1}^{8}\bar{E}_s^{*,n+1}\boldsymbol{f}_s \\ 0 \end{pmatrix} \\ &= \mathcal{A}^{-1} \begin{pmatrix} B^T\boldsymbol{f} \\ b \end{pmatrix} \end{aligned} \tag{A.52}$$

which means

$$\boldsymbol{a}_{i,j} = \bar{E}_{i,j}^{*,n+1}\boldsymbol{a}_0 + \sum_{s=1}^{8} \bar{E}_s^{*,n+1}\boldsymbol{a}_s$$

is the solution of (A.51) and $\boldsymbol{a}_0, \boldsymbol{a}_s$ only depends on the mesh information.

After that, we can use this reconstruction polynomial $W_{i,j}^{n+1}(x,y)$ to calculate the derivatives $\partial_x \boldsymbol{H}(\boldsymbol{U}^{n+1})$, $\partial_y \boldsymbol{H}(\boldsymbol{U}^{n+1})$. So, the line integral $\int_{\partial I_{i,j}} \widehat{\boldsymbol{H}}^{n+1} dl$ in the numerical flux (5.38) could be represented as a combination of unknown cell averages $\bar{E}^{*,n+1}$. Accordingly, the first order EIN scheme (5.37) follows as a linear system problem

$$\bar{\boldsymbol{U}}^{n+1}|I^{n+1}| - \tau \int_{\partial I} \widehat{\boldsymbol{H}}^{n+1} dl = \bar{\boldsymbol{U}}^{n}|I^{n}| + \tau \int_{\partial I} (-\widehat{\boldsymbol{F}}^{n} + \widehat{\boldsymbol{G}}^{n} - \widehat{\boldsymbol{H}}^{n}) dl, \quad \forall i, j. \tag{A.53}$$

For each conserved variables, the left side is a $N_x N_y \times N_x N_y$ matrix and the right side is a $N_x N_y \times 1$ vector.

References

[1] B. R. Bassett, J. M. Owen, T. A. Brunner, *Efficient smoothed particle radiation hydrodynamics II: Radiation hydrodynamics*, Journal of Computational Physics, 492 (2021), 109994.

[2] J. W. Bates, D. A. Knoll, W. J. Rider, R. B. Lowrie, V. A. Mousseauy, *On consistent time-integration methods for radiation hydrodynamics in the equilibrium diffusion limit: Low-energy-density regime*, Journal of Computational Physics, 167 (2001), 99-130.

[3] S. Bolding, J. Hansel, J. D. Edwards, J. E. Morel, R. B. Lowrie, *Second-order discretization in space and time for radiation-hydrodynamics*, Journal of Computational Physics, 338 (2017), 511-526.

[4] J. Cheng, C.-W. Shu, *A high order ENO conservative Lagrangian type scheme for the compressible Euler equations*, Journal of Computational Physics, 227 (2007), 1567-1596.

[5] J. Cheng, C.-W. Shu, *A third order conservative Lagrangian type scheme on curvilinear meshes for the compressible Euler equations*, Communications in Computational Physics, 4 (2008), 1008-1024.

[6] J. Cheng, C.-W. Shu, *Positivity-preserving Lagrangian scheme for multi-material compressible flow*, Journal of Computational Physics, 257 (2014), 143-168.

[7] J. Cheng, C.-W. Shu, Peng Song, *High order conservative Lagrangian schemes for one-dimensional radiation hydrodynamics equations in the equilibrium-diffusion limit*, Journal of Computational Physics, 421 (2020), 109724.

[8] J. M. Ferguson, J. E. Morel, R. Lowrie, *The equilibrium-diffusion limit for radiation hydrodynamics*, Journal of Quantitative Spectroscopy & Radiative Transfer, 202 (2017), 176-186.

[9] S. Gottlieb, C.-W. Shu, E. Tadmor, *Strong stability-preserving high-order time discretization methods*, SIAM review, 43 (2001), 89-112.

[10] S. Y. Kadioglu, D. A. Knoll, *A fully second order implicit/explicit time integration technique for hydrodynamics plus nonlinear heat conduction problems*, Journal of Computational Physics, 229 (2010), 3237-3249.

[11] S. Y. Kadioglu, D. A. Knoll, R. B. Lowrie, R. M. Rauenzahn, *A second order self-consistent IMEX method for radiation hydrodynamics*, Journal of Computational Physics, 229 (2010), 8313-8332.

[12] R. Kannan, M. Vogelsberger, F. Marinacci, R. McKinnon, R. Pakmor, V. Springel, *AREPO-RT: radiation hydrodynamics on a moving mesh*, Monthly Notices of the Royal Astronomical Society, 485 (2019), 117-149.

[13] N. Lei, J. Cheng, C.-W. Shu, *A high order positivity-preserving conservative WENO remapping method on 2D quadrilateral meshes*, Computer Methods in Applied Mechanics and Engineering, 373 (2021), 113497.

[14] P.-H. Maire, *A high-order cell-centered Lagrangian scheme for two-dimensional compressible fluid flows on unstructured meshes*, Journal of Computational Physics, 228 (2009), 2391-2425.

[15] D. Mihalas, B. Weibel-Mihalas, *Foundations of Radiation Hydrodynamics*, Oxford University Press, 1984.

[16] C. D. Munz, *On Godunov-type schemes for Lagrangian gas dynamics*, SIAM Journal on Numerical Analysis, 31 (1994), 17-42.

[17] S. Qamar, W. Ashraf, *Application of central schemes for solving radiation hydrodynamical models*, Computer Physics Communications, 184 (2013), 1349-1363.

[18] M. D. Sekora, J. M. Stone, *A hybrid Godunov method for radiation hydrodynamics*, Journal of Computational Physics, 229 (2010), 6819-6852.

[19] K.-M. Shyue, *A fluid-mixture type algorithm for barotropic two-fluid flow problems*, Journal of Computational Physics, 200 (2004), 718-748.

[20] W. Sun, S. Jiang, K. Xu, G. Cao, *Multiscale Simulation for the System of Radiation Hydrodynamics*, Journal of Scientific Computing, 85 (2020), 25.

[21] M. Tan, J. Cheng, C.-W. Shu, *Stability of high order finite difference and local discontinuous Galerkin schemes with explicit-implicit-null time-marching for high order dissipative and dispersive equations*, Journal of Computational Physics, 464 (2022), 111314.

[22] E. F. Toro, *Riemann solvers and numerical methods for fluid dynamics: a practical introduction*, Springer Science & Business Media, (2013).

[23] H. Wang, Q. Zhang, S. Wang, C.-W. Shu, *Local discontinuous Galerkin methods with explicit-implicit-null time discretizations for solving nonlinear diffusion problems*, Science China Mathematics, 63 (2020), 183-204.

[24] Y. Yang, L. Pan, W. Sun, *High-order gas-kinetic scheme for radiation hydrodynamics in equilibrium-diffusion limit*, arXiv preprint arXiv:2110.06557, (2021).

[25] X. Zhang, C.-W. Shu, *On positivity preserving high order discontinuous Galerkin schemes for compressible Euler equations on rectangular meshes*, Journal of Computational Physics, 229 (2010), 8918-8934.

[26] X. Zhang, C.-W. Shu, *Positivity preserving high order discontinuous Galerkin schemes for compressible Euler equations with source terms*, Journal of Computational Physics, 230 (2011), 1238-1248.

[27] X. Zhang, C.-W. Shu, *A minimum entropy principle of high order schemes for gas dynamics equations*, Numerische Mathematik, 121 (2012), 545-563

[28] J. Zhu, C.-W. Shu, *A new type of multi-resolution WENO schemes with increasingly higher order of accuracy*, Journal of Computational Physics, 375 (2018), 659-683.

[29] J. Zhu, C.-W. Shu, *A new type of multi-resolution WENO schemes with increasingly higher order of accuracy on triangular meshes*, Journal of Computational Physics, 392 (2019), 19-33.